



18 **Abstract**

19 This study evaluates the performance of four bulk-type microphysics schemes, Weather Research and
20 Forecasting (WRF) Double-Moment 6-class (WDM6), WRF Double-Moment 7-class (WDM7), Thompson,
21 and Morrison, focusing on hydrometeors and microphysics budgets in the WRF model version 4.1.3. Eight
22 snowstorm cases, which can be subcategorized as cold-low, warm-low, and air-sea interaction cases,
23 depending on the synoptic environment during the International Collaborative Experiment held at the
24 Pyeongchang 2018 Olympics and Winter Paralympic Games (ICE-POP 2018) field campaign, are selected.
25 All simulations present a positive bias in the simulated surface precipitation for cold-low and warm-low cases.
26 Furthermore, the simulations for the warm-low cases show a higher probability of detection score than
27 simulations for the cold-low and air-sea interaction cases even though the simulations fail to capture the
28 accurate transition layer for wind direction. WDM6 and WDM7 simulate abundant cloud ice for the cold-low
29 and warm-low cases, so snow is mainly generated by aggregation. Meanwhile, Thompson and Morrison
30 simulate insignificant cloud ice amounts, especially over the lower atmosphere, where cloud water is
31 simulated instead. Snow in Thompson and Morrison is mainly formed by the accretion between snow and
32 cloud water and deposition. The melting process is analyzed as a key process to generate rain in all schemes.
33 The discovered positive precipitation bias for the warm-low and cold-low cases can be mitigated by inefficient
34 melting using all schemes. The contribution of melting to rain production is reduced for the air-sea interaction
35 case with decreased solid-phase hydrometeors and increased cloud water in all simulations.

36 **Keywords:** Microphysics budgets, Hydrometeors, Snowfall, Bulk-type cloud microphysics, ICE-POP 2018.

37



38 1. Introduction

39 International Collaborative Experiments for Pyeongchang 2018 Olympic and Paralympic winter games (ICE-
40 POP 2018) field campaign was conducted over the Gangwon region, the northeastern part of the Korean
41 Peninsula during winter between 2017 and 2018. Various microphysical datasets in higher spatial and
42 temporal resolutions were collected during ICE-POP 2018 using X-band Doppler dual-polarization radar
43 (MXPoI), vertically pointing W-band Doppler cloud profiler (WProf), two dimensional video disdrometers
44 (2DVD) and PARTicle Size VELOCITY (PARSIVEL) disdrometers, etc. Furthermore, numerical weather
45 prediction using various high-resolution models around the world was conducted to support weather forecasts
46 during the Olympic winter games as part of the Forecast Demonstration Project efforts of World Weather
47 Research Program in World Meteorological Organization. The analysis of collected observed data and high-
48 resolution modeling information during ICE-POP 2018 can improve our understanding of the snowfall
49 formation mechanism and related cloud microphysics processes over the complex terrain along the
50 mountainous region over Korea (Kim et al., 2021a; Gehring et al., 2020b; Gehring et al., 2021; Lim et al.,
51 2020; Jeoung et al., 2020).

52 Over the past decades, comparisons of microphysics schemes for simulating convections have been
53 performed, either on idealized testbeds (Morrison and Grabowski, 2007; Morrison and Milbrandt, 2011; Bao
54 et al., 2019) or real-world testbeds (Liu and Moncrieff, 2007; Luo et al., 2010; Han et al., 2013; Min et al.,
55 2015; Das et al., 2021). Han et al. (2013) evaluated cloud microphysics schemes for simulating winter storms
56 over California using observations from a space-borne radiometer and a ground-based precipitation profiling
57 radar. Simulations using four different cloud microphysics, Goddard, Weather Research and Forecasting
58 (WRF) single-moment 6-class scheme (WSM6), Thompson, and Morrison, showed a large variation in the
59 simulated radiative properties. All schemes overestimated precipitating ice aloft, and thus, positive biases in
60 the simulated microwave brightness temperature were found. The Morrison scheme presented the greatest
61 peak reflectivity due to snow intercept parameters. Min et al. (2015) reported that the experiment with the
62 WRF double-moment 6-class (WDM6) scheme shows better agreement with the radar observations for
63 summer monsoon over the Korean Peninsula compared to WSM6. Das et al. (2021) performed numerical



64 simulations over southwest India and concluded that the WDM6 microphysics scheme better simulates the
65 vertical convection structure of deep convection storms than the Morrison scheme and the Milbrandt-Yau
66 double-moment scheme and compare favorably to radar observations.

67 The aforementioned studies compared simulated precipitation, reflectivity, and storm structures using
68 different microphysics schemes under real-convection testbeds (Han et al., 2013; Min et al., 2015; Das et al.,
69 2021). Although these studies attempted to evaluate model performance using possible radar measurements,
70 they did not suggest microphysics pathways affecting the superiority of model performance. Recently, a few
71 studies have analyzed major microphysical pathways to cloud hydrometeor production, i.e., precipitation
72 (McMillen and Steenburgh 2015; Fan et al., 2017; Vignon et al., 2019; Huang et al., 2020; Lim et al., 2020).
73 Through snowstorm simulations over the Great Salt Lake region, McMillen and Steenburgh (2015) reported
74 that WDM6 generates more graupel and less snow with more total precipitation than Thompson scheme. The
75 difference in graupel generation is due to WDM6's more efficient freezing of rain to graupel compared to
76 Thomson. The amount of simulated graupel and snow efficiently affects precipitation efficiency for the
77 selected snowstorm. Fan et al. (2017) simulated mesoscale squall line with eight cloud microphysics schemes
78 in the WRF model and identified processes that contribute to the large variability in the simulated cloud and
79 precipitation properties of the squall line. They found that the simulated precipitation rates and updraft
80 velocities present significant variability among simulations with different schemes. Differences in ice
81 microphysics processes and collision-coalescence parameterizations between the schemes affected the
82 simulated updraft velocity and surface rainfall variability. Lim et al. (2020) also analyzed the microphysical
83 pathway to generate hydrometeors using WSM6 and WDM6 and showed that abundant cloud ice generation
84 through the depositional process in both schemes can be a reason for the positive precipitation bias during the
85 winter season.

86 Although major microphysics processes have been explored in a certain convection environment in
87 previous studies, simulated hydrometeor profiles have not been evaluated with the observation. Therefore, we
88 cannot determine whether the analyzed microphysical pathway is plausible. The purpose of this study is to
89 compare simulated hydrometeors and microphysics budgets as well as precipitation using different bulk-type
90 cloud microphysics schemes and evaluate the results with the possible observations during the ICE-POP 2018



91 field campaign. Furthermore, our study aims to estimate which microphysical pathway is possible under a
92 certain synoptic circumstance, which can be feasible by evaluating hydrometeor profiles with the observations.
93 This study is organized as follows. Section 2 describes the observation data used in this study and model
94 design with the case description. Results and summary are presented in sections 3 and 4, respectively.

95

96 **2. Experimental setup**

97 **2.1. Case description**

98 The eight snowfall events during the ICE-POP 2018 field campaign are selected in our study. Kim et al. (2021a)
99 classified the eight cases into three categories, namely, cold-low, warm-low, and air-sea interaction, according
100 to synoptic characteristics. A widespread snowfall can occur over the northeastern part of Korea during the
101 passage of a low-pressure system (LPS) over the Korean Peninsula (Nam et al., 2014; Gehring et al., 2020b).
102 Snowfall cases, categorized as a cold-low type, occur when the LPS located in the north of the polar jet
103 produces precipitation in the middle of the Korean Peninsula. These cases are featured with the predominant
104 westerly flow from the ground level to the cloud top (Kim et al., 2021a). From the thorough visual inspection
105 of sea-level pressure pattern, radar composite images, and accumulated precipitation distribution at the ground,
106 CASES 1 and 3 are categorized as a cold-low type (Table 1).

107 When the LPS located in the south of the polar jet passes over the southern part of Korea, widespread
108 precipitation can occur over the southern and middle parts of the Korean Peninsula. Kim et al. (2021a)
109 classified snowfall cases occurring under this synoptic situation as a warm-low type. One of the most
110 significant characteristics of this pattern is the two different vertical layers (Tsai et al., 2018; Kim et al., 2018;
111 Kim et al., 2021a; Kim et al., 2021b): the deep system aloft (~10 km height) is associated with LPS widespread
112 precipitation with the westerly flow, whereas the other snowstorm below is associated with sea-effect snow
113 with the easterly or northeasterly flow (Kor'easterlies, hereafter) (Park et al., 2020). Thus, the seeder-feeder
114 effect is expected in this type of precipitation systems. This vertical structure is maintained until the LPS-
115 related widespread precipitation moves further east to the East Sea or Japan, followed by the shallow



116 precipitation system with the Kor'easterlies-induced snow. Five warm-low events, CASES 2, 4, 5, 6, and 8 in
117 Table 1 were identified during the field campaign.

118 Snowfall cases associated with the air-sea interaction occur, accompanied by the Siberian high expansion
119 toward Kaema Plateau and/or East Sea. As the cold air from the north flows over the warm East Sea, a snow
120 cloud is formed (Veals et al., 2019; Steenburgh and Nakai, 2020), and it is advected by the Kor'easterlies,
121 resulting in frequent snowfall over the northeastern part of Korea. The depth of the snowfall system is
122 generally shallower (less than ~3 km height) than other types and is determined by the depth of the
123 Kor'easterlies layer and the height of the thermal inversion layer above. The air-sea interaction is the most
124 frequent synoptic scenario to produce heavy snowfall in the northeastern part of the Korean Peninsula (Cheong
125 et al., 2006; Choi and Kim, 2010; Kim et al., 2021a). However, only one event, CASE 7 in Table 1, is identified
126 during the ICE-POP 2018 field campaign. Our study selects CASES 3, 6, and 7 as representative cases for the
127 cold-low, warm-low, and air-sea interaction categories, respectively. A more detailed explanation of the
128 characteristics of each category is provided in Kim et al. (2021a).

129 **2.2. Observation data**

130 The observed precipitation from the Korea Meteorological Administration Automatic Weather Station (AWS)
131 during the analysis period for CASE 3, CASE 6, and CASE 7 is shown in Figure 1. A heated tipping-bucket
132 gauge was located on each station. The forecast and analysis period for each case is noted in Table 1 with the
133 total accumulated rain [mm] and the maximum rain rates [mm h^{-1}] during the analysis period. The spatial
134 distribution of surface precipitation in CASE 3 is rather uniform (Fig. 1a), producing a maximum rain rate of
135 2.41 mm h^{-1} . For CASE 6, abundant precipitation amounts are shown in southeastern region and along the
136 coastal region (Figs. 1b). The maximum rain rate along the coastal region is shown in CASE 7 (air-sea
137 interaction). The observed maximum rain rate is 3.9 mm h^{-1} for CASE 6 and 4.87 mm h^{-1} for CASE 7. The
138 greatest amount of precipitation is observed with CASE 4 (warm-low), and the least one with CASE 3 (cold-
139 low) among the eight cases (Table 1).



140 Accurate measurement of precipitation by a heated tipping-bucket gauge is a challenge in windy
141 environment. Strong winds lead to severe undercatch of snowfall amount in particular for a solid precipitation
142 (Goodison et al., 1998; Thompson and Eidhammer, 2014; Kochendorfer et al., 2017; Smith et al., 2020). Other
143 sources of measurement uncertainty include sublimation or evaporation on the heated gauge funnel
144 (Rasmussen et al., 2012), orifice capping during heavy snowfall (Boudala et al., 2014), blowing snow (Geerts
145 et al., 2015), and representativeness of the observation particularly in the mountainous region. Hence, it should
146 be noted that the precipitation amount analyzed in this study may suffer from these sources of uncertainty,
147 likely resulting in less precipitation amount. Despite these limitations, this study takes an advantage of dense
148 network of heated tipping-bucket gauges, which was comprised of 129 stations within the studied area of
149 about $160 \times 200 \text{ km}^2$. In addition, all gauges were equipped with a single shield that improves catch efficiency
150 of snow in windy condition (Kochendorfer et al., 2017).

151 During the ICE-POP 2018 field campaign, remote-sensing, and in situ measurements for cloud properties
152 were performed over the northeastern part of South Korea. The Gangneung-Wonju National University (GWU)
153 marked with a closed red square in Figure 1a represents the coastal observation site. DaeGwallyeong regional
154 Weather office (DGW), MayHills Supersite (MHS), and BoKwang 1-ri Community Center (BKC) are the
155 mountain observation sites, which are represented as an open circle and a closed triangle sign in Figure 1a.
156 PARSIVEL disdrometers (Löffler-Mang and Joss, 2000; Tokay et al., 2014) at the GWU and DGW sites
157 provide the frequency distributions of particle fall velocity as functions of diameter at the surface; thus, we
158 can obtain the information about the surface precipitation type for each representative case, as shown in Figure
159 2. At the coastal site, GWU, a mixture of snow and liquid-type precipitation is measured for CASE 3. CASE
160 6 is characterized by the liquid-type and graupel-like precipitation, and CASE 7 consists of the liquid-type
161 precipitation. At the mountain site, DGW, a mixture of liquid-type precipitation with snow and graupel is
162 observed in all cases, but a more intense signal of the liquid-type precipitation is seen in CASE 7.

163 The MXPOL radar measurement, located at the GWU site, provides the classified hydrometeor
164 information along the direction between MHS and GWU. Figure 3 shows the area of hydrometeor types in
165 which the hourly average fraction is larger than the threshold. The period is selected for the peak time of the



166 domain-averaged rain for each case. The radar-classified hydrometeors are 8 hydrometeor types based on
167 the algorithm proposed by Besic et al. (2016, 2018): crystals (CR), aggregates (AG), light rain (LR), rain (RN),
168 rimed ice particles (RP), wet snow (WS), ice hail and high-density graupel (IH), and melting hail (MH). The
169 hydrometeors are not drawn over the region, where radar echoes are absent.

170 CR is the primary hydrometeor type, and AG is between 1.5 and 3.0-km level in CASE3 (Fig. 3a). For
171 CASE6, CR is also the major hydrometeor type over the entire observational region. A small portion of AG
172 exists around the coastal GWU site at the 0.5-km level (Fig.3b). Hydrometeors are mainly classified into CR,
173 AG with a small portion of RP above the 0.5-km level, and WS/LR below the 0.5-km level from the
174 observation for CASE 7 (Fig. 3c). The freezing level is drawn using the radiosonde observations at BKC site
175 on 09 UTC 22 Jan, 00 UTC 08 Mar, and 15 UTC 15 MAR for each case. The retrieved wind fields (cross-
176 barrier and vertical wind) from multiple surveillance Doppler radars (Liou and Chang, 2009; Tsai et al., 2018)
177 are also represented in Figure 3. The wind fields are the hourly averaged ones during the 1-h time window,
178 centered at the maximum precipitation time. The westerly winds generally blow from mountains to the ocean
179 and become stronger with higher altitude in CASE 3. Both CASESs 6 and 7 show the transition zone of wind
180 fields, northeasterly below and southwesterly above. In general, the flow patterns well follow the overall
181 characteristic of winds for three types of precipitation systems (see Kim et al. 2021a).

182 **2.3. Model design**

183 The Advanced Research WRF model version 4.1.3 (Skamarock et al., 2008) is used for simulations. The WRF
184 model is a nonhydrostatic, compressible model with an Arakawa-C grid system and has several options for
185 each physics parameterization. The model grids consist of three nested domains with a horizontal grid spacing
186 of 9, 3, 1 km (Fig. 4). The 65 vertical levels are configured with a 50-hPa model top. Table 2 shows the
187 summary of the model configuration, including the number of model grids, the physics parameterization used,
188 and initial/boundary conditions for model integration. The Kain-Fritsch (Kain and Fritsch, 1990; Kain, 2004)
189 scheme is only applied to the outer domain of the 9-km resolution domain. The model forecast and analysis
190 periods for each case are listed in Table 1. The model results are evaluated over the Yeongdong area of
191 northeastern South Korea during the analysis period, represented as a dotted square in Figure 4.



192 Four cloud microphysics parameterizations, namely, WDM6 (Lim and Hong 2010), WRF Double-
193 Moment 7-class (WDM7) (Bae et al. 2019), Thompson (Thompson et al. 2008), and Morrison (Morrison et
194 al. 2005), are used in our study. WDM6 and WDM7 schemes include the corrections for the numerical errors
195 in ice microphysics parameterizations (Kim and Lim, 2021) and for cloud evaporation and melting processes
196 (Lei et al., 2020). WDM6, Thompson, and Morrison parameterizations include five hydrometeor types such
197 as cloud water, rain, ice, snow, and graupel. WDM7 is developed on the basis of WDM6 by adding the
198 prognostic variable of hail mixing ratio. WDM6 and WDM7 predict both number concentration and the
199 mixing ratio for liquid particles but only the mixing ratio for solid-phase hydrometeors. Thompson predicts
200 the number concentration and the mixing ratio for ice and rain but only the mixing ratio for other hydrometeors.
201 In Morrison, the number concentration and the mixing ratio are predicted for all hydrometeors, except for
202 cloud water, for which only the mixing ratio is predicted. There exist the aerosol-aware versions of Thompson
203 and Morrison schemes in the WRF model. However, we perform the model simulations using Thompson and
204 Morrison schemes, which do not include the aerosol activation processes; thus, two schemes do not predict
205 the cloud water number concentration. Table 3 shows the prognostic variables for each microphysics scheme.
206 The tested parameterizations are full or partially double-moment schemes, as shown in Table 3. For the
207 microphysics budget analysis, the name of the source/sink terms in each microphysics scheme, differently
208 designated, is matched, as shown in Table 4. For example, the cloud water condensation/evaporation process
209 from all microphysics schemes is identically denoted as QCCON.

210

211 **3. Results**

212 **3.1. Cold-low case**

213 The simulation results for cold-low cases are presented in this section. Figure 5 shows the statistical skill
214 scores of bias, root mean square error (RMSE), probability of detection (POD), and false alarm ratio (FAR)
215 for the simulated precipitation using the WDM6, WDM7, Thompson, and Morrison schemes. We adopt the
216 threshold value of 0.05 mm h^{-1} to judge the existence of precipitation when calculate POD and FAR. The



217 calculation method of POD and FAR follows the study of Rezacova et al. (2009). All microphysics
218 parameterizations overestimate the surface precipitation amount. Thompson and Morrison simulations show
219 better skill scores in bias, RMSE, and FAR, compared to WDM6 and WDM7. The accumulated precipitation
220 during the analysis period for CASE 3, the representative case of the cold-low type, is shown in Figures 6a–
221 d. All schemes simulate the precipitation as a type of snow and rain over the northeastern part of the domain.
222 WDM6 and WDM7 simulate more liquid rain at the surface precipitation than Morrison and Thompson.
223 Simulated hydrometeor types at the surface are compared qualitatively with measurements using PARSIVEL
224 disdrometers (Fig. 2). In CASE 3, the simulated hydrometeor types are snow and rain over the coast and
225 mountains in all schemes (Figs. 6a–d). Although graupel-type precipitation is not predicted at the surface in
226 all schemes, the overall feature matches well with the observation (Figs. 2a and d).

227 When the strongest domain-averaged precipitation intensity is observed, the simulated hydrometeors and
228 wind are compared with the retrieved ones from radars along the cross-section between GWU and MHS sites
229 (Figs. 3a and 7a–d). For the comparison analysis, hydrometeor types of CR, AG, and IH from the retrievals
230 can be regarded as cloud ice, snow, and hail in the model. The hydrometeor type of RP can be corresponded
231 to graupel in the model. RN and MH can be considered rain in the model, and LR as cloud water or rain. WS
232 is not predicted by any of the microphysics schemes verified in our study. WDM6 and WDM7 simulate cloud
233 ice over the entire region of the cross-section above 2-km level. Furthermore, cloud ice is predicted, even near
234 the mountain top, with a substantial snow amount. However, both schemes miss the observed snow near GWU
235 site. Thompson and Morrison also simulate sufficient snow mass, showing its maximum near the mountain
236 top. However, cloud ice is not simulated with both schemes. This is because Thompson and Morrison schemes
237 efficiently transfer cloud ice to snow at the cut-off diameter of 200 and 250 μm , therefore the schemes keep
238 all cloud ice size relatively small. Over the mountain top where cloud ice is shown in WDM6 and WDM7,
239 cloud water is simulated with Morrison and Thompson instead. More cloud ice with WDM6 and WDM7 can
240 be also confirmed in the time-domain averaged vertical profiles of hydrometeors (Fig. 8). As shown in Figures
241 8a and b, the vertical distributions of hydrometeors from WDM6 and WDM7 are similar, except hail. WDM7
242 simulates more hail as much as decreased snow. Thompson rarely produces ice and shows the largest snow



243 amount among the schemes used in the experiments. Morrison simulates cloud ice in layers between 3-and 6-
244 km levels. Meanwhile, the sum of cloud ice and snow, drawn in a red line, shows a similar amount in all
245 schemes. Consistently with the hydrometeor distribution shown from the cross-section, Thompson and
246 Morrison produce more cloud water below 4-km level than WDM6 and WDM7 (Figs. 8c and d). In all
247 experiments, the simulated winds blow from the inland to the ocean, consistently shown from the observation
248 (Figs. 3a and 7a–d). Meanwhile, the simulated winds are weaker than the observation over the mountainous
249 areas.

250 The relative contribution of microphysics processes in the production of each hydrometeor is compared
251 among experiments in Figure 9. The production rate of microphysical processes is averaged over the same
252 analysis domain and duration, as considered in the precipitation and hydrometeor analysis shown in Figures
253 5 and 6. The absolute values of every production rate to generate or dissipate a certain hydrometeor are
254 summed, and each production rate is divided by the sum to generate a percentage. The positive rates in Figure
255 9 indicate source processes for the hydrometeor, and the negative rates indicate sink ones. The contribution
256 of sedimentation could be indirectly estimated from the hydrometeor mixing ratio and cloud microphysics
257 budget amount. The cloud condensation nuclei (CCN) activation process (QCGEN) is the main source of
258 cloud water in WDM6 and WDM7 (Figs. 9a–b). Meanwhile, cloud water in Thompson and Morrison is
259 primarily generated by QCCON due to the absence of QCGEN (Figs. 9c–d). Note that we use the non-aerosol-
260 aware version of the Thompson and Morrison scheme, which excludes aerosols and related microphysics
261 processes. The collision/coalescence between cloud water and other hydrometeors (QCACR, QCACS, and
262 QCACG) is the main sink for cloud water in all schemes. Besides these accretions, evaporation is another
263 major sink of cloud water in WDM6 and WDM7. Most of the rain is produced by melting from solid-phase
264 hydrometeors (QRMLT) (Figs. 9e–h) in all experiments and consumed by the evaporation process (QRCON),
265 except for Thompson.

266 The deposition/sublimation of water vapor to cloud ice (QIDEP) is the primary source of cloud ice (Figs.
267 9i–l). Cloud ice decreases as it is converted into snow due to the auto-conversion process (QSAUT) and
268 collision/coalescence process with snow (QIACS). The main processes to generate or deplete cloud ice are



269 identical in all microphysics schemes. However, the absolute magnitude of QIDEP in WDM6 and WDM7,
270 that is, approximately 1.4 g kg^{-1} , is greater than that in Morrison and Thompson, approximately 0.05 g kg^{-1} ,
271 leading to more cloud ice generation. In WDM6 and WDM7, most of the snow is produced by QSAUT and
272 QIACS, but in Morrison, it is produced by QCACS and deposition from water vapor to snow (QSDEP) (Figs.
273 9 m–o). QCACS is the primary source of snow in Thompson as well (Fig. 9p). Snow is depleted by a melting
274 process (QSMLT) in all simulations. The accretion between snow and hail (QSACH) is also the primary sink
275 of snow in WDM7. Meanwhile, graupel is mainly produced by the accretion process, QCACG, in WDM6(7)
276 and Morrison. However, in Thompson, graupel is mainly produced by the freezing process (QGFRZ) and
277 QCACS. WDM7, predicting hail additionally, shows that the collision/coalescence between graupel and hail
278 (QGACH) and QSACH are the major processes for hail generation. Meanwhile, Jang et al. (2021) showed
279 that QGACH and QSACH can be eliminated by applying the mass-weighted terminal velocity for hail
280 following the method by Dudhia et al. (2008); thus, the hail generation considerably decreases.

281 Except for the major sinks of graupel and snow, QGACH and QSACH, the responsible microphysical
282 processes for generating hydrometeors in WDM6 and WDM7 are similar. The inclusion of aerosols in the
283 microphysics processes causes the difference in major source/sink of cloud water, which can be seen from the
284 comparison between WDM6(7) and Morrison/Thompson. In addition, more efficient cloud ice and inefficient
285 cloud water production in WDM6(7), compared to others, cause the difference in the primary microphysics
286 processes for snow production. Kim et al. (2021a) estimated possible microphysical processes from the
287 measured particle size distribution and diameter for the cold-low case during ICE-POP 2018. Both aggregation
288 and riming are analyzed as major processes to produce snow at the mountain site. Our analysis shows that
289 aggregation is preferred in WDM6(7) and riming in Thompson and Morrison at the top of the mountain (Figs.
290 7a–d). In addition, the enhanced melting of solid-phase particles in WDM6(7), compared to Thompson,
291 produces much rain, resulting in a larger positive bias of simulated precipitation.

292 **3.2. Warm-low case**

293 Simulated precipitation, hydrometeors, and microphysics budgets are compared for the warm-low cases in
294 this section. The warm-low category includes five cases such as CASES 2, 4, 5, 6, and 8. Overall, all
12



295 simulations in the warm-low category show better POD and FAR than those in the cold-low category, except
296 FAR for CASE 8. Consistent with the simulations for the cold-low category, all simulations in the warm-low
297 category present a positive bias of surface precipitation, except CASE 4 with WDM7 (Fig. 5). WDM6 overall
298 shows the best bias scores. Morrison shows the best POD score, but the worst bias, RMSE, and FAR, by
299 producing abundant precipitation, except for CASE 5. All simulations show the worst bias and RMSE scores
300 for CASE 5 among the warm-low cases. WDM6, Thompson, and Morrison simulate the surface precipitation
301 type as rain and snow (Figs. 6e, g, and h). However, WDM7 simulates abundant hail-type precipitation over
302 the southeastern part of the analysis domain. Jang et al (2021) noted that WDM7 generates too much hail
303 regardless of the simulated convections. The area receiving the snow-type precipitation is confined in a narrow
304 mountain region with WDM7 (Fig. 6f). The simulated hydrometeor types in all simulations are inconsistent
305 with the observations, especially over the coastal region. The observation certainly shows graupel-like
306 precipitation over the coastal region (Fig. 2b).

307 Figures 7e–h shows the simulated hydrometeors and wind fields for CASE 6 when the strongest domain-
308 averaged precipitation intensity is observed. The simulated cloud ice appears just above the freezing level in
309 WDM6 and WDM7. WDM7 simulates the freezing level lower than other schemes, which is not consistent
310 with the observation (Figs. 7f and 3b). Meanwhile, Thompson and Morrison simulate a large amount of snow
311 above the surface with an absence of cloud ice because these schemes only allow the relatively small size of
312 cloud ice. WDM7, Thompson, and Morrison simulate cloud water below the 0.5-km level over the coast. The
313 vertical profiles of the time-domain averaged hydrometeors present more snow and cloud water with
314 Thompson and Morrison (Fig. 10cd). Figure 10 also shows that WDM6 and WDM7 simulate more cloud ice
315 between the 10-km level and surface than other schemes. Morrison produces cloud ice between the 6- and 12-
316 km levels, and Thompson simulates a little cloud ice amount. However, the sum of snow and cloud ice amount
317 is greatest in Thompson. All cloud ice in Thompson scheme is relatively smallest, therefore its mixing ratio
318 can be nearly always an order of magnitude or more less than other schemes. Kim et al. (2021a) mentioned
319 that snowfall cases belonging to the warm-low category show the deepest system and precipitation are
320 enhanced by the seeder–feeder mechanism with two different precipitation systems divided by wind fields,



321 easterly below and westerly above. However, the transition layer of wind direction in all simulations is located
322 at the higher latitude, relative to the observed layer (compare Figs. 7e–h and 3b), which can cause a deficiency
323 in simulating related microphysical mechanisms.

324 The relative contribution of microphysical processes to generate each hydrometeor among the schemes
325 is compared in Figure 11. QCGEN and QCCON are the primary sources for cloud water in WDM6(7) and
326 Thompson/Morrison, respectively. The contribution of QRWET, responsible for generating rain, is reduced
327 with WDM7 for the warm-low case, compared to the cold-low case. QRMLT is still the primary source of
328 rain in all simulations (Figs. 11 e–h). The major sinks and sources of the liquid hydrometeors are similar
329 between the warm-low and cold-low cases. The responsible microphysical processes for cloud ice formation
330 and depletion are also identical to those for the cold-low case (Figs. 11i–l). The main source of cloud ice is
331 QIDEP in all simulations. The magnitude of QIDEP in WDM6 and WDM7 is 5.5 g kg^{-1} , which is
332 approximately 10 times larger than that of Morrison and Thompson, leading to an abundant production of
333 cloud ice.

334 The melting processes (QSMLT, QGMLT, and QHMLT) are the primary sinks of solid-phase
335 precipitating particles such as snow, graupel, and hail in all simulations. The relative contribution of melting
336 for the warm-low case, CASE 6, is greater than that for the cold-low case, CASE 3, due to the warm
337 environment and the extended vertical range of solid-phase hydrometeors (Figs. 10m–u). All simulations show
338 that the magnitude of QRMLT in CASE 6 is approximately 10 times larger than that in CASE 3. The melting
339 process can largely affect rain production, resulting in surface precipitation in the warm-low case. The
340 contribution of QCACS to snow generation is significantly decreased in Thompson and Morrison in the warm-
341 low case compared to the cold-low case. This is because of the reduced cloud water in CASE 6 with Thompson
342 and Morrison, compared to the CASE 3. In both schemes, cloud water generation is suppressed in the warm-
343 low case. Even though both QSAUT and QIACS are still the major sources of snow production in WDM6(7),
344 the contribution of QSAUT decreases, and that of QIACS increases in WDM6 and WDM7 in the warm-low
345 case compared to the cold-low case. There is no distinct discrepancy for the key microphysical processes of
346 graupel (and hail) formation and depletion between the warm-low and cold-low cases.



347 **3.3. Air-sea interaction case**

348 Statistical skill scores for the simulated precipitation are presented in Figure 5 for the air-sea interaction case.
349 Only one case, CASE 7, is classified as an air-sea interaction category during the ICE-POP 2018 field
350 campaign, presenting a negative bias. Overall, Morrison shows the best skill scores for the simulated
351 precipitation. The POD from simulations with WDM6 and WDM7 show the worst scores due to the missing
352 precipitation events over the southwestern part of the analysis domain (Figs. 1c and 6i, j). The precipitation
353 system, which is initiated by air-mass transformation over the East Sea, propagates to inland areas by the
354 easterly winds. Therefore, the precipitation area is restricted in the eastern area of the Korean Peninsula and
355 intense precipitation is presented along the coast in both the observation and simulations (Figs. 6i–l). WDM6
356 and WDM7 simulate abundant solid-phase precipitation compared with the simulations with Thompson and
357 Morrison. In addition, WDM7 produces hail-type precipitation over the coast. The precipitation type simulated
358 with WDM6 and WDM7 does not match with the observed types, especially over the coast (Figs. 2 and 6i–l).
359 Observation shows pure liquid-type precipitation, but both simulations produce excess solid-phase
360 precipitation.

361 The simulated hydrometeor distribution and wind fields over the cross-section are compared to the
362 observations (Figs. 3 and 7i–l). When the strongest domain-averaged precipitation intensity is observed, all
363 simulations produce a significant amount of cloud water below the 3-km level. A large amount of cloud water
364 in the simulations can be also confirmed in the time-domain averaged vertical profiles of hydrometeors (Fig.
365 12). In all simulations, simulated hydrometeors are confined to below the 4-km level. WDM6 and WDM7
366 produce the largest amount of cloud water and cloud ice/snow. The experiment with Morrison simulates more
367 rain than other simulations (Fig. 12d). WDM6 and WDM7 simulate cloud ice with some snow and graupel
368 below the 2-km level, which is consistent with the observation in which CR, AG, and RP are seen (Figs. 3 and
369 7i, j). However, the region with the graupel (RP in the observation) is shifted to the coastal region in WDM6
370 and WDM7, generating excess solid-phase precipitation over the coast. Consistent with other cases,
371 Thompson and Morrison do not simulate cloud ice at the maximum precipitation time. Morrison simulates
372 snow between the surface and 2-km level, representing its maximum at the coastal GWU site (Fig. 8l). All



373 experiments show westerly wind over the ocean and coastal area, indicating that they fail to simulate the
374 Kor'easterlies, which is the most important dynamical characteristics of the air-sea interaction category.

375 Figure 13 shows the relative contribution of microphysical processes for CASE 7. Unlike the cold-low
376 and warm-low cases, cloud water is mainly depleted by QCACR in Thompson and Morrison due to decreased
377 snow production in the air-sea interaction case. The primary source and sink for cloud water are not changed
378 in WDM6 and WDM7. In all simulations, the relative contribution of QRMLT in the generation of rain
379 decreases, and the contribution of cloud water-to-rain processes such as QCACR, QRAUT, and QRWET
380 increases. In particular, QCACR and QRAUT are the main sources of rain in Thompson, and QCACR in
381 Morrison. For cloud ice, QIDEP and the generation of ice by nucleation and CCN activation (QIGEN) are
382 analyzed as the major sources in all simulations. The contribution of QIGEN in cloud ice production increases
383 compared to cold-low and warm-low cases. In all simulations, the relative contribution of QCACS to the
384 formation of snow increases due to increased cloud water generation, and those of QIACS and QSAUT
385 decrease with the decreased cloud ice generation. However, QIACS and QSAUT in both WDM6 and WDM7
386 are still major sources of snow. Both schemes simulate abundant cloud ice compared to Thompson and
387 Morrison in CASE 7 as well. In Morrison, the contribution of QSDEP to snow formation is significantly
388 reduced in the air-sea interaction case, unlike the cold-low and warm-low cases. Several microphysics
389 processes are involved in graupel formation with Thompson for the air-sea interaction case, but the formed
390 graupel amount is insignificant.

391

392 **4. Summary**

393 This study evaluates the performance of the four microphysics parameterizations, WDM6, WDM7, Thompson,
394 and Morrison, which have been widely used as cloud microphysics options in the WRF model, in simulating
395 snowfall events during the ICE-POP 2018 field campaign. Eight snowfall events, classified into three
396 categories (cold-low, warm-low, and air-sea interaction), depending on the synoptic characteristics, are
397 selected. The evaluation is conducted focusing on the simulated hydrometeors, microphysics budgets, wind



398 fields, and precipitation using the measurement data from MXPoL radar, multiple surveillance Doppler radars,
399 PARSIVEL disdrometers, and AWS. Most simulations show a deficiency of a positive bias in the simulated
400 precipitation for the cold-low and warm-low cases. The simulations for the air-sea interaction case present a
401 negative bias and show the best bias score. Overall, the modeled precipitation for the warm-low cases shows
402 a better POD score than that for the cold-low and air-sea interaction cases.

403 The simulated hydrometeor types at the surface for the cold-low case are snow and rain over both coastal
404 and mountainous regions, regardless of the microphysics schemes, which is consistent with the observed
405 features. Both WDM6 and WDM7 simulate a abundant amount of cloud ice and snow, especially over the
406 mountain top and its downslope region when the strongest precipitation intensity is observed. The retrievals
407 from the radar also show abundant cloud ice and snow over the downslope region of the mountain top.
408 Thompson and Morrison simulate sufficient snow amount; however, both do not produce cloud ice over the
409 downslope region, because these schemes keep all cloud ice relatively small, compared to WDM6 and WDM7.
410 In all experiments, the simulated winds blow from the inland to the ocean, as observed in the Doppler radar-
411 retrieved one. Most rain mixing ratio is produced by melting in all experiments. The primary processes that
412 generate or deplete cloud ice are identical in all microphysical schemes, which are the deposition for the
413 formation and conversion to snow or collision/coalescence for depletion. Snow is mainly generated by
414 aggregation in WDM6 and WDM7, but the accretion between snow and cloud water and deposition is mainly
415 generated in Thompson and Morrison.

416 For the warm-low case, all experiments mainly produce rain and snow-type surface precipitation over
417 the coastal and mountainous areas. WDM7 predicts abundant hail-type precipitation. The simulated
418 hydrometeor types in all simulations are inconsistent with the observations, which shows graupel-like
419 precipitation especially over the coastal region. WDM6 and WDM7 simulate the abundant cloud ice near the
420 coast site when the maximum precipitation is observed. Meanwhile, Morrison and Thompson simulate
421 abundant snow over the corresponding region. Although the simulated precipitation skill scores for the warm-
422 low category are the best among all simulated categories, all simulations have a problem, the lower wind-
423 transition layer, compared to the observed-transition layer. Through the microphysics budget analysis, it is



424 found that the major sources and sinks of hydrometeors are similar between the cold-low and warm-low cases.
425 Meanwhile, the magnitude of melting is significantly enhanced in warm-low cases compared to cold-low
426 cases, due to the warmer environment and more available solid-phase hydrometeors. The relative contribution
427 of collision/coalescence between cloud water and snow to produce snow is decreased compared to cold-low
428 cases in the simulations with Thompson and Morrison, which is due to the reduced cloud water. For the air-
429 sea interaction case, WDM6 and WDM7 simulate surface precipitation as a solid-phase type along the coast,
430 which is inconsistent with the observation. This is because WDM6 and WDM7 produce excessive cloud ice
431 amount with graupel/snow over the coast. In addition, none of the experiments simulate the low-level
432 Kor'easterlies. Unlike the cold-low and warm-low cases, simulations for the air-sea interaction case produce
433 abundant cloud water. Therefore, rain is greatly generated by cloud collision/coalescence of cloud water, not
434 primarily from melting.

435 More cloud ice generation with WDM6 and WDM7 and more cloud water generation with the Morrison
436 and Thompson schemes are distinct in all cases. Therefore, the major microphysical processes to generate
437 snow are significantly related with cloud ice in WDM6 and WDM7, and with cloud water in Morrison and
438 Thompson. Thompson (or Morrison) scheme transfers the cloud ice to snow at the diameter of 200 (or 250)
439 μm , therefore more snow exists relative to WDM6 and WDM7 schemes, in which the maximum allowable
440 diameter of cloud ice is 500 μm . Melting is the major process to produce rain in warm-low and cold-low cases.
441 Therefore, the positive precipitation bias revealed from the warm-low and cold-low cases can be mitigated by
442 modulating the melting efficiency in all schemes. Microphysics budget analysis shows that the inclusion of
443 the prognostic variable of CCN number concentration changes the major source of cloud water production.
444 CCN activation is the major process to produce cloud water with WDM6 and WDM7, with the CCN number
445 concentration serving as a prognostic variable, but the condensation is the major process for cloud water
446 generation with Morrison and Thompson. Our study also shows that the additional prognostic variable of hail
447 has no advantage in simulating precipitation and hydrometeor profiles and produces excessive hail at the
448 surface for the snowfall event that occurs over the complex terrain region in the eastern part of the Korean
449 Peninsula.



450

451 *Code and data availability.* The WRF model version 4.1.3 is available at [https://github.com/wrf-](https://github.com/wrf-model/WRF/releases)
452 [model/WRF/releases](https://github.com/wrf-model/WRF/releases) (last access: January 2022). The ERA-Interim reanalysis data from the European Centre
453 for Medium-Range Weather Forecasts (ECMWF) for initial and boundary conditions is available at
454 <https://apps.ecmwf.int/datasets/data/interim-full-daily/levtype=pl/> and
455 <https://apps.ecmwf.int/datasets/data/interim-full-daily/levtype=sfc/> (last access: October 2019). The model
456 codes and scripts and that cover every data and figure processing action for all the results reported in this
457 paper are available at https://zenodo.org/record/5876054#.YefSK_5BwuU. The observational data such as
458 Parsivel and MXPoI radar are available via <http://dx.doi.org/10.5067/GPMGV/ICEPOP/APU/DATA101> and
459 <https://doi.org/10.1594/PANGAEA.918315>. Model outputs are available upon the request (Jeong-Su Ko via
460 jsko@knu.ac.kr).

461

462 *Author contributions.* JK designed and performed the model simulations and analysis under the supervision
463 of KL. KL and JK wrote the manuscript with substantial contributions from all co-authors. KK processed the
464 observational data. KL, GL, AB, and GT contributed to the scientific discussions and gave constructive advice.
465 KK and AB carried out the PARSIVEL and Radar measurements.

466

467 *Competing interests.* The authors declare that they have no conflict of interest.

468

469 *Special issue statement.* This article is part of the special issue “Winter weather research in complex terrain
470 during ICE-POP 2018 (International Collaborative Experiments for PyeongChang 2018 Olympic and
471 Paralympic winter games) (ACP/AMT/GMD inter-journal SI)”. It is not associated with a conference.

472



473 *Funding.* This work was supported by the National Research Foundation of Korea (NRF) grant funded by the
474 Korean government (MSIT) (No. 2021R1A4A1032646)

475

476 *Acknowledgments.* The authors are greatly appreciative to the participants of the World Weather Research
477 Program Research Development Project and Forecast Demonstration Project, International Collaborative
478 Experiments for Pyeongchang 2018 Olympic and Paralympic winter games (ICE-POP 2018), hosted by the
479 Korea Meteorological Administration. The authors would also like to thank Josué Gehring, Nikola Besic, and
480 Alfonso Ferrone for their contribution to the operation and maintenance of the MXPoI radar and for providing
481 the hydrometeor classification product (<https://doi.org/10.1594/PANGAEA.918315>, Besic et al., 2018;
482 Gehring et al., 2020a; Gehring et al., 2021) and to thank Petersen Walter A and Ali Tokay for their contribution
483 to the Parsivel data product (Petersen et al., 2019).

484



485 **References**

- 486 Bao, J.-W., Michelson, S. A., and Grell, E. D.: Microphysical process comparison of three microphysics
487 parameterization schemes in the WRF model for an idealized squall-line case study, *Mon. Weather Rev.*,
488 147, 3093-3120, <https://doi.org/10.1175/MWR-D-18-0249.1>, 2019.
- 489 Basic, N., Gehring, J., Praz, C., Figueras i Ventura, J., Grazioli, J., Gabella, M., Germann, U., and Berne, A.:
490 Unraveling hydrometeor mixtures in polarimetric radar measurements, *Atmos. Meas. Tech.*, 11, 4847–
491 4866, <https://doi.org/10.5194/amt-11-4847-2018>, 2018.
- 492 Boudala, F. S., Isaac, G. A., Rasmussen, R., Cober, S. G., and Scott, B.: Comparison of snowfall
493 measurements in complex terrain made during the 2010 Winter Olympics in Vancouver, *Pure Appl.*
494 *Geophys.*, 171, 113-127, <https://doi.org/10.1007/s00024-012-0610-5>, 2014.
- 495 Chen, F., and Dudhia, J.: Coupling an advanced land surface–hydrology model with the Penn State–NCAR
496 MM5 modeling system. Part I: Model implementation and sensitivity, *Mon. Weather Rev.*, 129, 569–
497 585, [https://doi.org/10.1175/1520-0493\(2001\)129<0569:CAALSH>2.0.CO;2](https://doi.org/10.1175/1520-0493(2001)129<0569:CAALSH>2.0.CO;2), 2001.
- 498 Cheong, S.-H., Byun, K.-Y., and Lee, T.-Y.: Classification of snowfalls over the Korean Peninsula based on
499 developing mechanism, *Atmosphere*, 16, 33-48, 2006.
- 500 Das, S. K., Hazra, A., Deshpande, S. M., Krishna, U. M., and Kolte, Y. K.: Investigation of cloud
501 microphysical features during the passage of a tropical mesoscale convective system: Numerical
502 simulations and X-band radar observations, *Pure Appl. Geophys.*, 178, 185–204,
503 <https://doi.org/10.1007/s00024-020-02622-w>, 2021.
- 504 Dee, D. P., and coauthors: The ERA-Interim reanalysis: configuration and performance of the data
505 assimilation system. *Q. J. R. Meteorol. Soc.*, 137, 553–597, <https://doi.org/10.1002/qj.828>, 2011.



- 506 Dudhia, J., Hong, S. Y., Lim, K. S.: A new method for representing mixed-phase particle fall speeds in bulk
507 microphysics parameterization, *J. Meteorol. Soc. Jpn.*, 86, 33-44, <https://doi.org/10.2151/jmsj.86A.33>,
508 2008.
- 509 Fan, J., and coauthors: Cloud-resolving model intercomparison of an MC3E squall line case: Part 1-
510 Convective updrafts, *J. Geophys. Res. Atmos.*, 122, 9351–9378, <https://doi.org/10.1002/2017JD026622>,
511 2017.
- 512 Geerts, B., Yang, Y., Rasmussen, R., Haimov, S., and Pokharel, B.: Snow growth and transport patterns in
513 orographic storms as estimated from airborne vertical-plane dual-doppler radar data, *Mon. Weather*
514 *Rev.*, 143, 644-665, <https://doi.org/10.1175/MWR-D-14-00199.1>, 2015.
- 515 Gehring, J., Ferrone, A., Billault-Roux, A. C., Besic, N., and Berne, A.: Radar and ground-level measurements
516 of precipitation during the ICE-POP 2018 campaign in South-Korea, *PANGAEA*,
517 <https://doi.org/10.1594/PANGAEA.918315>, 2020a.
- 518 Gehring, J., Oertel, A., Vignon, É., Jullien, N., Besic, N., and Berne, A.: Microphysics and dynamics of
519 snowfall associated with a warm conveyor belt over Korea, *Atmos. Chem. Phys.*, 20, 7373–7392,
520 <https://doi.org/10.5194/acp-20-7373-2020>, 2020b.
- 521 Gehring, J., Ferrone, A., Bilault-Roux, A.-C., Besic, N., Anh, K. D., Lee, G., and Berne, A.: Radar and ground-
522 level measurements of precipitation collected by the École Polytechnique Fédérale de Lausanne during
523 the International Collaborative Experiments for PyeongChang 2018 Olympic and Paralympic winter
524 games. *Earth Syst. Sci. Data*, 13, 417–433, <https://doi.org/10.5194/essd-13-417-2021>, 2021.
- 525 Goodison, B. E., Louie P. Y. T., and Yang, D.: WMO solid precipitation measurement intercomparison, 1998.
- 526 Han, M., Braun, S. A., Matsui, T., and Williams, C. R.: Evaluation of cloud microphysics schemes in
527 simulations of a winter storm using radar and radiometer measurements, *J. Geophys. Res. Atmos.*, 118,
528 1401–1419, <https://doi.org/10.1002/jgrd.50115>, 2013.



- 529 Hong, S. Y., Noh, Y., and Dudhia, J.: A new vertical diffusion package with an explicit treatment of
530 entrainment processes, *Mon. Weather Rev.*, 134, 2318–2341, <https://doi.org/10.1175/MWR3199.1>,
531 2006
- 532 Huang, Y., Wang, Y., Xue, L., Wei, X., Zhang, L., and Li, H.: Comparison of three microphysics
533 parameterization schemes in the WRF model for an extrem rainfall event in the coastal metropolitan
534 City of Guangzhou, China, *Atmos. Res.*, 240, 104939, <https://doi.org/10.1016/j.atmosres.2020.104939>,
535 2020.
- 536 Iacono, M. J., Delamere, J. S., Mlawer, E. J., Shephard, M. W., Clough, S. A., and Collins, W. D.: Radiative
537 forcing by long-lived greenhouse gases: Calculations with the AER radiative transfer models, *J.*
538 *Geophys. Res.*, 113, D13103, <https://doi.org/10.1029/2008JD009944>, 2008.
- 539 Jang, S., Lim, K. S. S., Ko, J., Kim, K., Lee, G., Cho, S. J., Ahn, K. D., and Lee, Y. H.: Revision of WDM7
540 microphysics scheme and evaluation for precipitating convection over the Korean peninsula, *Remote*
541 *Sens.*, 13, 3860, <https://doi.org/10.3390/rs13193860>, 2021.
- 542 Jiménez, P. A., Dudhia, J., González-Rouco, J. F., Navarro, J., Montávez, J. P., and García-Bustamante, E.:
543 A revised scheme for the WRF surface layer formulation, *Mon. Weather Rev.*, 140, 898–918,
544 <https://doi.org/10.1175/MWR-D-11-00056.1>, 2012.
- 545 Jeoung, H., Liu, G., Kim, K., Lee, G., and Seo, E.-K.: Microphysical properties of three types of snow clouds:
546 implication for satellite snowfall retrievals, *Atmos. Chem. Phys.*, 20, 14491–14507,
547 <https://doi.org/10.5194/acp-20-14491-2020>, 2020.
- 548 Kain, J. S. and Fritsch, J. M.: A one-dimensional entraining/detraining plume model and its application in
549 convective parameterization, *J. Atmos. Sci.* 47:2784–2802, 1990.
- 550 Kain, J. S.: The Kain–Fritsch convective parameterization: an update, *J. Appl. Meteorol. Climatol.*, 43, 170–
551 181, [https://doi.org/10.1175/1520-0450\(2004\)043<0170:TKCPAU>2.0.CO;2](https://doi.org/10.1175/1520-0450(2004)043<0170:TKCPAU>2.0.CO;2), 2004.



- 552 Kim, Y. J., Kim, B. G., Shim, J. K., and Choi, B. C.: Observation and numerical simulation of cold clouds
553 and snow particles in the Yeongdong region, *Asia-Pacific J. Atmos. Sci.*, 54, 499–510,
554 <https://doi.org/10.1007/s13143-018-0055-6>, 2018.
- 555 Kim, K., Bang, W., Chang, E., Tapiador, F. J., Tsai, C., Jung, E., and Lee, G.: Impact of wind pattern and
556 complex topography on snow microphysics during International Collaborative Experiment for
557 PyeongChang 2018 Olympic and Paralympic winter games (ICE-POP 2018). *Atmos. Chem. Phys.*, 21,
558 11955–11978, <https://doi.org/10.5194/acp-21-11955-2021>, 2021a.
- 559 Kim, Y. J., In, S. R., Kim, H. M., Lee, J. H., Kim, K. R., Kim, S., and Kim, B. G.: Sensitivity of snowfall
560 characteristics to meteorological conditions in the Yeongdong region of Korea, *Adv. Atmos. Sci.*, 38,
561 413–429, <https://doi.org/10.1007/s00376-020-0157-9>, 2021b.
- 562 Kim, K. B., and Lim, K.-S. S.: The numerical error in WDM6 and its impacts on the simulated precipitating
563 convections, AOGS 18h Annual Meeting, Asia Oceanic Geoscience Society, AS23-A005, 2021.
- 564 Kochendorfer, J., and coauthors: Analysis of single-Alter-shielded and unshielded measurements of mixed
565 and solid precipitation from WMO-SPICE, *Hydrol. Earth Syst. Sci.*, 21, 3525–3542,
566 <https://doi.org/10.5194/hess-21-3525-2017>, 2017.
- 567 Lei, H., Guo, J., Chen, D., and Yang, J.: Systematic bias in the prediction of warm-rain hydrometeors in the
568 WDM6 microphysics scheme and modifications, *J. Geophys. Res.*, 125,
569 <https://doi.org/10.1029/JD030756>, 2020.
- 570 Lim, K.S. S., Chang, E.-C., Sun, R., Kim, K., Tapiador, F. J., and Lee, G.: Evaluation of simulated winter
571 precipitation using WRF-ARW during the ICE-POP 2018 field campaign, *Wea. Forecasting*, 35, 2199–
572 2213, <https://doi.org/10.1175/WAF-D-19-0236.1>, 2020.
- 573 Liu, C., and Moncrieff, M. W.: Sensitivity of cloud-resolving simulations of warm-season convection to cloud
574 microphysics parameterizations, *Mon. Weather Rev.*, 135, 2854–2868,
575 <https://doi.org/10.1175/MWR3437.1>, 2007.



- 576 Liou, Y.-C., and Chang, Y.-J.: Variational multiple-doppler radar three-dimensional wind synthesis method
577 an dits impacts on thermodynamic retrieval, *Mon. Weather Rev.*, 137, 3992–4010,
578 <https://doi.org/10.1175/2009MWR2980.1>, 2009.
- 579 Luo, Y., Wang, Y., Wang, H., Zheng, Y., and Morrison, H.: Modeling convective-stratiform precipitation
580 processes on a Mei-Yu front with the Weather Research and Forecasting model: Comparison with
581 observations and sensitivity to cloud microphysics parameterizations, *J. Geophys. Res.*, 115,
582 <https://doi.org/10.1029/2010JD013873>, 2010.
- 583 McMillen, J. D., and Steenburgh, W. J.: Impact of microphysics parameterizations on simulations of the 27
584 October 2010 Great Salt Lake-effect snowstorm, *Wea. Forecasting*, 30, 136–152,
585 <https://doi.org/10.1175/WAF-D-14-00060.1>, 2015.
- 586 Min, K.-H., Choo, S., Lee, D., and Lee, G.: Evaluation of WRF cloud microphysics schemes using radar
587 observations, *Wea. Forecasting*, 30, 1571–1589, <https://doi.org/10.1175/WAF-D-14-00095.1>, 2015.
- 588 Morcrette, J., Barker, H. W., Cole, J. N. S., Iacono, M. J., and Pincus, R.: Impact of a new radiation package,
589 McRad, in the ECMWF integrated forecasting system, *Mon. Weather Rev.*, 136, 4773–4798,
590 <https://doi.org/10.1175/2008MWR2363.1>, 2008.
- 591 Morrison, H., and Grabowski, W. W.: Comparison of bulk and bin warm-rain microphysics models using a
592 kinematic framework, *J. Atmos. Sci.*, 64, 2839–2861, <https://doi.org/10.1175/JAS3980>, 2007.
- 593 Morrison, H. and Milbrandt, J.: Comparison of two-moment bulk microphysics schemes in idealized supercell
594 thunderstorm simulations, *Mon. Weather Rev.* 139, 1103–1130,
595 <https://doi.org/10.1175/2010MWR3433.1>, 2011
- 596 Nam, H.-G., Kim, B.-G., Han, S.-O., Lee, C., and Lee, S.-S.: Characteristics of easterly-induced snowfall in
597 Yeongdong and its relationship to air-sea temperature difference, *Asia Pac. J. Atmos. Sci.*, 50, 541–552,
598 <https://doi.org/10.1007/s13143-014-0044-3>, 2014.



- 599 Park, S. K., and Park, S.: On a flood-producing coastal mesoscale convective storm associated with the
600 kor'easterlies: Multi-Data analyses using remotely-sensed and in-situ observations and storm-scale
601 model simulations, *Remote Sens.*, 12, 1–25, <https://doi.org/10.3390/RS12091532>, 2020.
- 602 Petersen, Walter A and Ali Tokay: GPM Ground Validation Autonomous Parsivel Unit (APU) ICE
603 POP [indicate subset used]. Dataset available online from the NASA Global Hydrology Resource
604 Center DAAC, Huntsville, Alabama, U.S.A.,
605 <http://dx.doi.org/10.5067/GPMGV/ICEPOP/APU/DATA101>, 2019.
- 606 Rasmussen, R., and coauthors: How well are measuring snow: The NOAA/FAA/NCAR winter precipitation
607 test bed, *Bull. Am. Meteorol. Soc.*, 93, 811-829, <https://doi.org/10.1175/BAMS-D-11-00052.1>, 2012.
- 608 Rezacova, D., , P. Zacharov, , and Z. Sokol: Uncertainty in the area-related QPF for heavy convective
609 precipitation, *Atmos. Res.*, **93**, 238–246, doi:10.1016/j.atmosres.2008.12.005, 2009
- 610 Skamarock, W. C., and coauthors: A description of the advanced research WRF version 3 (2008) NCAR
611 Technical Note, NCAR, Boulder, CO, 2008.
- 612 Smith, C. D., Ross, A., Kochendorfer, J., Earle, M. E., Wolff, M., Buisán, S., Roulet Y,-A., and Laine, T.:
613 Evaluation of the WMO solid precipitation intercomparison experiment (SPICE) transfer functions for
614 adjusting the wind bias in solid precipitation measurements, *Hydrol. Earth Syst. Sci.*, 24,4025-4043,
615 <https://doi.org/10.5194/hess-24-4025-2020>, 2020.
- 616 Steenburgh, W. J., and Nakai, S.: Perspectives on sea-and lake-effect precipitation from Japan's "Gosetsu
617 Chitai", *Bull. Am. Meteorol. Soc.*, 101, E58–E72, <https://doi.org/10.1175/BAMS-D-18-0335.1>, 2020.
- 618 Thompson, G., and Eidhammer, T.: A study of aerosol impacts on clouds and precipitation development in a
619 large winter cyclone, *J. Atmos. Sci.*, 71, 3636-3658, <https://doi.org/10.1175/JAS-D-13-0305.1>, 2014.



- 620 Tsai, C., Kim, K., Liou, Y., Lee, G., and Yu, C.: Impacts of topography on airflow and precipitation in the
621 Pyeongchang area seen from Multiple-Doppler Radar observations, *Mon. Weather Rev.*, 146, 3401–
622 3424, <https://doi.org/10.1175/MWR-D-17-0394.1>, 2018.
- 623 Veals, P. G., Steenburgh, W. J., Nakai, S., and Yamaguchi, S.: Factors affecting the inland and orographic
624 enhancement of sea-effect snowfall in the Hokuriku region of Japan, *Mon. Weather Rev.*, 147, 3121–
625 3143, <https://doi.org/10.1175/MWR-D-19-0007.1>, 2019.
- 626 Vignon, É., Besic, N., Jullien, N., Gehring, J., Berne, A.: Microphysics of snowfall over coastal east antarctica
627 simulated by polar WRF and observed by radar, *J. Geophys. Res. Atmos.*, 124, 11452-11476,
628 <https://doi.org/10.1029/2019JD031028>, 2019.
- 629



630 **Figure and Table captions**

631 **Table 1.** Eight selected snowfall events during the International Collaborative Experiment held at the
632 Pyeongchang 2018 Olympics and Winter Paralympic Games (ICE-POP 2018) field campaign and their
633 characteristics, obtained from the automatic weather station (AWS) by the Korea Meteorological
634 Administration (KMA). Forecast and analysis periods are also noted.

635 **Table 2.** Summary of the Weather Research and Forecasting (WRF) model configurations.

636 **Table 3.** Four bulk-type cloud microphysics parameterizations and their prognostic variables. The existence
637 of prognostic variables in each parameterization is denoted with the symbol “o” (existence) or “x”
638 (nonexistence). N_x and Q_x represent the number concentration and mixing ratio of a hydrometeor, X. The
639 subscript, C, R, I, S, G, and H, indicates cloud water, rain, cloud ice crystal, snow, graupel, and hail,
640 respectively.

641 **Table 4.** List of symbols for cloud microphysical processes in each microphysics scheme and their meaning.
642 The symbol used differently in each scheme is reconciled in our study, addressed in the row, “Notation.”

643 **Figure 1.** Observed accumulated precipitation amount [mm] (a) for 21-h from 0300 UTC 22 to 0000 UTC 23
644 January (CASE 3), (b) for 29-h from 0500 UTC 07 to 1000 UTC 08 March (CASE 6), and (c) for 10-h from
645 0800 UTC 15 to 1800 UTC 15 March (CASE 7), obtained from the AWS. The location of one coastal site,
646 Gangneung-Wonju National University (GWU) and three mountain sites, BoKwang 1-ri Community Center
647 (BKC), DaeGwallyeong regional Weather office (DGW) and MayHills Supersite (MHS) is noted in Figure
648 1(a). **Figure 2.** Normalized frequency of the measured precipitation particle fall velocity as a function of
649 diameters at GWU (upper panel) and DGW (lower panel) sites. (a), (d) are for CASE 3, (b), (e) for CASE 6,
650 and (c), (f) for CASE 7 during the analysis period. The solid lines represent the relationship between the fall
651 velocity and diameter for rain (the power law fit the Gunn and Kinzer (1949) data (Atlas et al., 1973)), dendrite
652 (derived from the observed data (Lee et al., 2015)), graupel, and hail (derived from the observed data
653 (Heymsfield et al., 2018)) at sea level.

654 **Figure 3.** Area of hydrometeor types in which hourly average fraction of hydrometeors is larger than the
655 threshold indicated. Hydrometeor types are derived from X-band Doppler dual polarization radar (MXPo)



656 along the direction between MHS and GWU sites at (a) 10 UTC 22 Jan (CASE 3), (b) 23 UTC 07 Mar (CASE
657 6), and (c) 14 UTC 15 Mar (CASE 7). Eight hydrometeor categories such as crystal (CR), aggregate (AG),
658 rimed particle (RP), ice hail/graupel (IH), melting hail (MH), wet snow (WS), light rain (LR), and rain (RN)
659 are identified. The Green shade represents the terrain. The flows along the cross-section, retrieved from
660 multiple Doppler radars, are also drawn in each figure and the vertical component of the arrows are upward
661 air motion. The flows and classified hydrometeors are the hourly averaged ones.

662 **Figure 4.** Model domain consisted of the three nested domains with 9-3-1-km resolutions centered on the
663 Korean peninsula. Shading indicates the terrain height [m] above the sea level and latitudes and longitudes
664 are denoted in the margins. The analysis domain is denoted with a dotted square inside of the innermost
665 domain, d03.

666 **Figure 5.** Statistical skill scores of bias, root mean square error (RMSE), probability of detection (POD), and
667 false alarm ratio (FAR) for the simulated precipitation, with respect to the AWS observation. The units of bias
668 and RMSE shown in Figures 5(a) and (b) are [mm]. White, black, yellow, and blue-colored bars represent the
669 results for the simulations with the WDM6, Thompson, and Morrison schemes. The cold-low, warm-low, and
670 air-sea interaction cases are shaded in blue, red, and green color.

671 **Figure 6.** Accumulated precipitation [mm] of the simulations using different cloud microphysics
672 parameterizations during the analysis period. (a)–(d) are for CASE 3, (b), (e) for CASE 6, and (c), (f) for
673 CASE 7 during the analysis period. (a)–(d) are for CASE 3, (e)–(h) for CASE 6, and (j)–(l) for CASE7. The
674 simulations in the first and second columns are conducted with the WDM6 and WDM7 schemes. The ones in
675 the third and fourth columns are conducted with the Thompson and Morrison schemes. Red, blue, and black
676 contours represent the snow, graupel, and hail-type precipitation at the surface. The contour intervals for snow,
677 graupel, and hail are 5, 10, and 3 mm.

678 **Figure 7.** Terrain and the simulated hydrometeor mixing ratio along the cross-section between GWU and
679 MHS sites for (a)–(e) CASE 3, (f)–(j) CASE 6, and (k)–(o) CASE 7. From the left column, figures indicate
680 the simulation results with the WDM6, WDM7, Thompson, and Morrison schemes. Shaded green and blue
681 indicate the cloud water and ice mixing ratios, respectively. Red, blue, and black-solid contours are for the
682 snow, graupel, and hail mixing ratios. The contour levels are in 0.1 g kg^{-1} increments and the contour labels



683 are in $0.1\text{--}0.2\text{ g kg}^{-1}$ increments. The gray solid line represents the 0°C line. The wind fields are overlaid at
684 the same time.

685 **Figure 8.** Time-domain averaged vertical hydrometeor mixing ratio profiles from the simulations using (a)
686 WDM6, (b) WDM7, (c) Thompson, and (d) Morrison schemes for CASE 3. The averaged time and domain
687 are the same as Figure 6. The sum of snow and cloud ice mixing ratios is drawn with a red line in all
688 simulations.

689 **Figure 9.** Relative contribution of time-domain averaged production term during the analysis period. From
690 the left column, figures indicate the simulation results with the WDM6, WDM7, Thompson, and Morrison
691 schemes. (a)–(d) are the terms for cloud water, (e)–(h) for rain, (i)–(l) for cloud ice, (m)–(p) for snow, and
692 (q)–(t) for graupel, and (u) for hail. The hail is only predicted in WDM7.

693 **Figure 10.** Same as Figure 8 but representing the results for CASE 6.

694 **Figure 11.** Same as Figure 9 but representing the results for CASE 6.

695 **Figure 12.** Same as Figure 8 but representing the results for CASE 7.

696 **Figure 13.** Same as Figure 9 but representing the results for CASE 7.

697

698

699



700 **Table 1.** Eight selected snowfall events during the International Collaborative Experiment held at the
 701 Pyeongchang 2018 Olympics and Winter Paralympic Games field campaign and their characteristics, obtained
 702 from the Automatic Weather Station by the Korea Meteorological Administration. Forecast and analysis
 703 periods are also noted.

704

	Forecast Period [UTC]	Analysis Period [UTC]	Accumulated Precipitation [mm]	Maximum Rain Rate [mm h ⁻¹]	Synoptic Feature
CASE 1	2017.11.24.1200–26.1200	2017.11.24.20000–26.0000	32.09	13.23	Cold Low
CASE 2	2017.12.23.1200–24.1800	2017.12.23.2000–24.1200	18.60	6.45	Warm Low
CASE 3	2018.01.22.0000–23.0600	2018.01.22.0300–23.0000	6.03	2.41	Cold Low
CASE 4	2018.02.27.1800–03.01.0000	2018.02.27.2300–28.1800	57.12	10.19	Warm Low
CASE 5	2018.03.04.0000–05.1200	2018.03.04.0800–05.0900	55.17	13.65	Warm Low
CASE 6	2018.03.07.0000–08.1200	2018.03.07.0500–08.1000	33.07	3.93	Warm Low
CASE 7	2018.03.15.0000–16.0000	2018.03.15.0800–15.1800	25.52	4.87	Air-sea interaction
CASE 8	2018.03.20.1200–21.1800	2018.03.20.1800–21.1400	25.83	3.186	Warm Low

705



706 **Table 2.** Summary of the Weather Research and Forecasting (WRF) model configuration.

707

	WRF v4.1.3			Reference
	Domain 1	Domain 2	Domain 3	
Number of grid ($x \times y \times z$)	$169 \times 169 \times 65$	$294 \times 348 \times 65$	$330 \times 339 \times 65$	
Cumulus	Kain-Fritsch			Kain and Fritsch, 1990; Kain, 2004
PBL	Yonsei University Scheme			Hong et al., 2006
Surface layer	Revised MM5 Monin-Obukhov scheme			Jiménez et al., 2012
Land surface	Unified Noah Land Surface Model			Chen and Dudhia 2001
Long/short wave radiation	Rapid Radiative Transfer Model for General Circulation Models			Iacono et al., 2008; Morcrette et al., 2008
Initial/boundary conditions	ERA-interim 0.75 Degree			Dee et al., 2011

708



709 **Table 3.** Four bulk-type cloud microphysics parameterizations and their prognostic variables. The existence
 710 of prognostic variables in each parameterization is denoted with “O” (existence) or “X” (nonexistence). N_x
 711 and Q_x represent the number concentration and mixing ratio of a hydrometeor, X. The subscript, C, R, I, S,
 712 G, and H, indicates cloud water, rain, cloud ice crystal, snow, graupel, and hail, respectively.
 713

Parameterization (Reference)	N_C	Q_C	N_R	Q_R	N_I	Q_I	N_S	Q_S	N_G	Q_G	N_H	Q_H
WDM6 (Lim and Hong, 2010)	O	O	O	O	X	O	X	O	X	O	X	X
WDM7 (Bae et al., 2018)	O	O	O	O	X	O	X	O	X	O	X	O
Thompson (Thompson et al., 2008)	X	O	O	O	O	O	X	O	X	O	X	X
Morrison (Morrison et al., 2005)	X	O	O	O	O	O	O	O	O	O	X	X

714



715 **Table 4.** List of symbols for cloud microphysical processes in each microphysics scheme and their meaning.

716 The symbol used differently in each scheme is reconciled in our study, addressed in the row, “Notation.”

717

Hydrometeor	Notation	Source/sink processes for each microphysics scheme				Meaning
		WDN6	WDM7	Thompson	Morrison	
Cloud water	QCCON	pcond	pcond	prw_vcd	pcc	Condensation/evaporation of cloud water
	QCGEN	pcact	pcact	-	-	CCN activation
	QRAUT	praut, prevp_s	praut, prevp_s	prr_wau	prc	Conversion from cloud water to rain
	QCFRZ	pihtf, pihmf	pihtf, pihmf	pri_wfz, pri_hmf	mnucce, pihmf	Freezing of cloud water
	QCACR	pracw	pracw	prr_rcw	pra	Accretion between cloud water and rain
	QCACI	-	-	-	psacwi	Accretion between cloud water and ice
	QCACS	paacw(T≤0°C)	paacw(T≤0°C)	prs_scw, prg_scw	psacws,pgsacw	Accretion between cloud water and snow
	QCACG	paacw(T≤0°C)	paacw(T≤0°C)	prg_gcw	psacwg	Accretion between cloud water and graupel
	QCACH	-	Phacw	-	-	Accretion between cloud water and hail
	QCWET	paacw, paacw(T≥0°C)	paacw, paacw, phacw(T≥0°C)	-	-	Wet growth and shedding
	QCMUL	-	-	-	qmults, qmultg	Ice multiplication
QCMLT	pimlt	pimlt	prw_uml	-	Melting to cloud water	
Rain	QRAUT	praut, prevp_s	praut, prevp_s	prr_wau	prc	Conversion from cloud water to rain
	QRCON	prevp	prevp	prv_rev	pre	Condensation/evaporation of rain
	QCACR	pracw	pracw	prr_rcw	pra	Accretion between cloud water and rain
	QRACI	piacr	piacr	prr_rci	piacr, piacrs	Accretion between rain and ice



	QRACS	psacr, pseml	psacr, pseml	pr_rcs	pracs	Accretion between rain and snow
	QRACG	pgacr, pgeml	pgacr, pgeml	pr_rcg	pracg	Accretion between rain and graupel
	QRACH	-	phacr, pheml	-	-	Accretion between rain and hail
	QRFRZ	pgrfz	Pgrfz	pri_rfz, prg_rfz	mnuccr, phsmf, pghmf	Freezing of rain
	QRMUL	-	-	-	qmultr, qmultrg	Ice multiplication by rain
	QRMLT	psmlt, pgmlt	psmlt, pgmlt, phmlt	pr_r_sml, pr_r_gml	pimlt, psmlt, pgmlt	Melting to rain
	QRWET	paacw, paacw(T≥0°C)	paacw, paacw, phacw(T≥0°C)	-	-	Wet growth and shedding
Cloud ice	QIGEN	pigen	pigen	pri_iha, pri_inu	mnuccd	Ice nucleation
	QIDEP	pidep	pidep	pri_ide	prd, eprd	Deposition/sublimation of ice
	QIMUL	-	-	pri_ihm	qmults, qmultr, qmultg, qmultrg	Ice multiplication
	QIFRZ	pihmf, pihtf	pihmf, pihtf	pri_wfz, pri_hmf, pri_rfz	mnuccc, pihmf	Freezing to ice
	QSAUT	psaut	psaut	prs_iau	prci	Conversion to snow
	QCACI	-	-	-	psacwi	Accretion between cloud water and ice
	QRACI	praci	praci	pri_rci	praci, pracis	Accretion between rain and ice
	QIACS	psaci	psaci	prs_sci	prai	Accretion between ice and snow
	QIACG	pgaci	pgaci	-	-	Accretion between ice and graupel



	QIACH	-	phaci	-	-	Accretion between ice and hail
	QIMLT	pimlt	pimlt	prw_iml	-	Melting from ice
Snow	QSAUT	psaut	psaut	prs_iau	prci	Conversion to snow
	QSDEP	psdep	psdep	prs_sde, prs_ide	prds, eprds	Deposition/sublimation of snow
	QSMUL	-	-	prs_ihm	-	Ice multiplication
	QSFRZ	-	-	-	pshmf	Freezing to snow
	QGAUT	pgaut	pguat	-	-	Conversion to graupel
	QCACS	paacw(T≤0°C)	paacw(T≤0°C)	prs_scw, prg_scw	psacws, pgsacw	Accretion between cloud water and snow
	QRACS	psacrqs, pracs, pseml	psacrqs, pracs, pseml	prs_rcs	pracs, psacr	Accretion between rain and snow
	QIACS	Psaci	psaci	prs_rci	prai	Accretion between ice and snow
	QSACG	-	-	-	-	Accretion between snow and graupel
	QSACH	-	phacs	-	-	Accretion between snow and hail
	QSMILT	psmlt	psmlt	prr_sml	psmlt	Melting from snow
	QRACI	piacrqs, praciqs	piacrqs, praciqs	-	piacrs, racis	Accretion between rain and ice
	QSEVP	psevp	psevp	-	evpms	Evaporation of melting snow
Graupel	QGAUT	pgaut	pgaut	-	-	Conversion to graupel
	QGDEP	pgdep	pgdep	prg_gde	prdg, eprdg	Deposition/sublimation of graupel
	QGMUL	-	-	prg_ihm	-	Ice multiplication
	QGFRZ	pgfrz	pgfrz	prg_rfz	mnucrr, pghmf	Freezing to graupel
	QCACG	paacw(T≤0°C)	paacw(T≤0°C)	prg_gcw	psacwg	Accretion between cloud water and graupel
	QRACG	pgacr, pgeml	pgacrqg, pgeml, pracg	prg_gcr	pracg	Accretion between rain and graupel
	QIACG	pgaci	pgaci	-	-	Accretion between ice and graupel



	QSACG	-	-	-	-	Accretion between snow and graupel
	QGACH	-	phacg	-	-	Accretion between graupel and hail
	QGMLT	pgmlt	pgmlt	prg_gml	pgmlt	Melting from graupel
	QCACS	-	-	prg_scw	pgsacw	Accretion between cloud water and snow
	QRACS	piacrqg, praciqg	piacrqg, praciqg	prg_rci	pgracs	Accretion between rain and snow
	QRACI	pracs, psacrqg	pracs, psacrqg	prg_rcs	-	Accretion between rain and ice
	QGEVP	pgevp	pgevp	-	evpmg	Evaporation of melting graupel
	QHAUT	-	phuaut	-	-	Conversion to hail
Hail	QHAUT		phuaut			Conversion to hail
	QHDEP		phdep			Deposition/sublimation of hail
	QCACH		phacw($T \leq 0^\circ\text{C}$)			Accretion between cloud water and hail
	QRACH		phacr, pheml			Accretion between rain and hail
	QIACH		phaci			Accretion between ice and hail
	QSACH		phacs			Accretion between snow and hail
	QGACH		phacg			Accretion between graupel and hail
	QHMLT		phmlt			Melting from hail
	QHEVP		phevp			Evaporation of melting hail
	QRACG		pgacrqh, pracg			Accretion between rain and graupel to hail

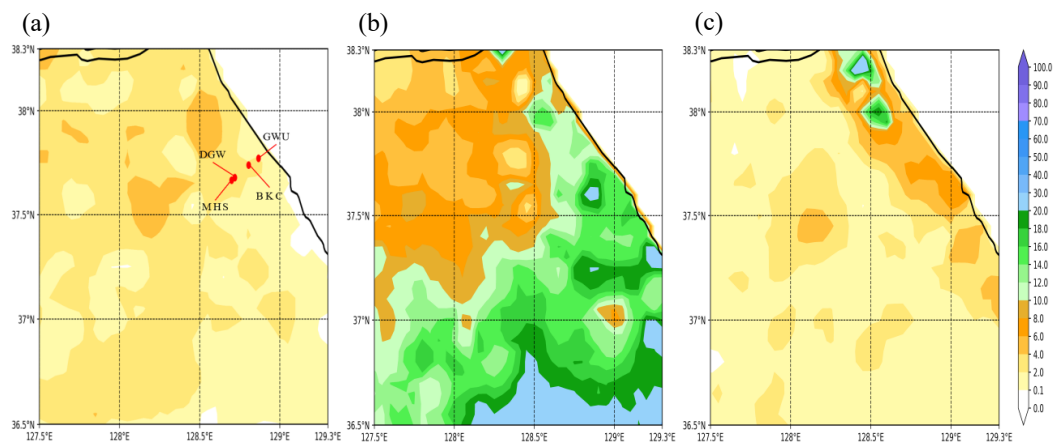
718

719



720 **Figure1.** Observed accumulated precipitation amount [mm] (a) for 21-h from 0300 UTC 22 to 0000 UTC 23
721 January (CASE 3), (b) for 29-h from 0500 UTC 07 to 1000 UTC 08 March (CASE 6), and (c) for 10-h from
722 0800 UTC 15 to 1800 UTC 15 March (CASE 7), obtained from the AWS. The location of one coastal site,
723 Gangneung-Wonju National University (GWU) and three mountain sites, BoKwang 1-ri Community Center
724 (BKC), DaeGwallyeong regional Weather office (DGW) and MayHills Supersite (MHS) is noted in Figure
725 1(a).

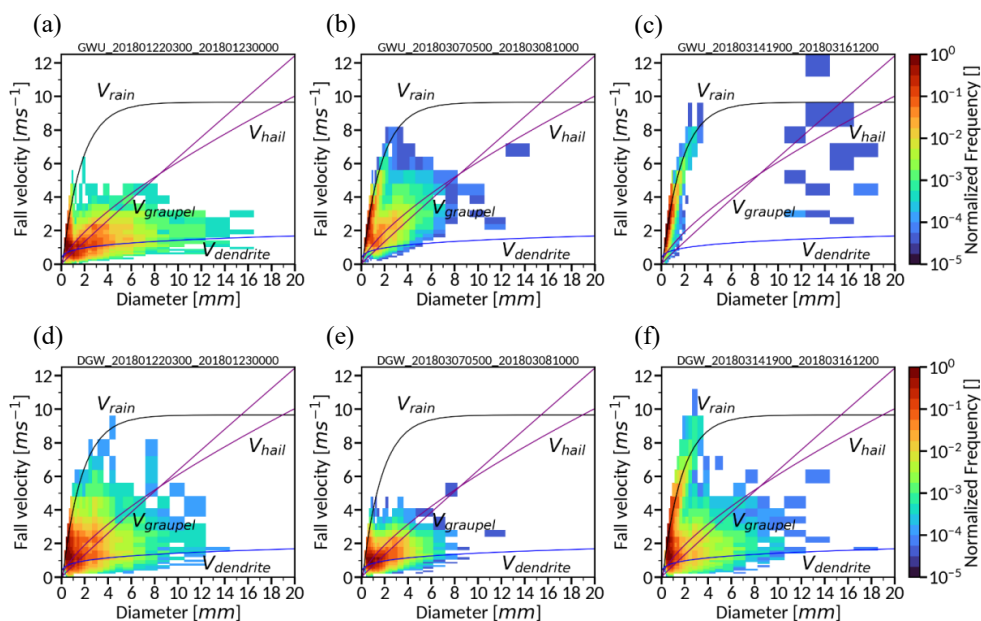
726
727





728 **Figure 2.** Normalized frequency of the measured precipitation particle fall velocity as a function of diameters
729 at GWU (upper panel) and DGW (lower panel) sites. (a), (d) are for CASE 3, (b), (e) for CASE 6, and (c), (f)
730 for CASE 7 during the analysis period. The solid lines represent the relationship between the fall velocity and
731 diameter for rain (the power law fit the Gunn and Kinzer (1949) data (Atlas et al., 1973)), dendrite (derived
732 from the observed data (Lee et al., 2015)), graupel, and hail (derived from the observed data (Heymnsfield et
733 al., 2018)) at sea level.

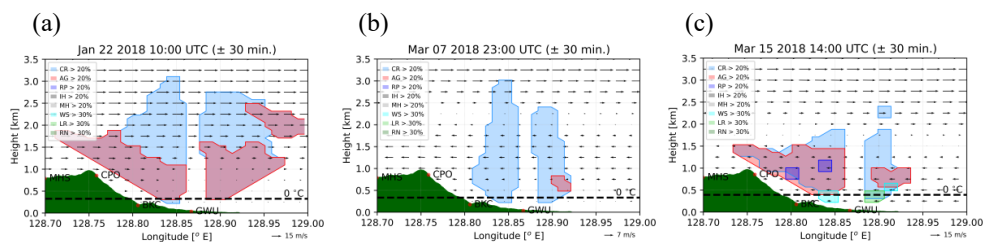
734
735





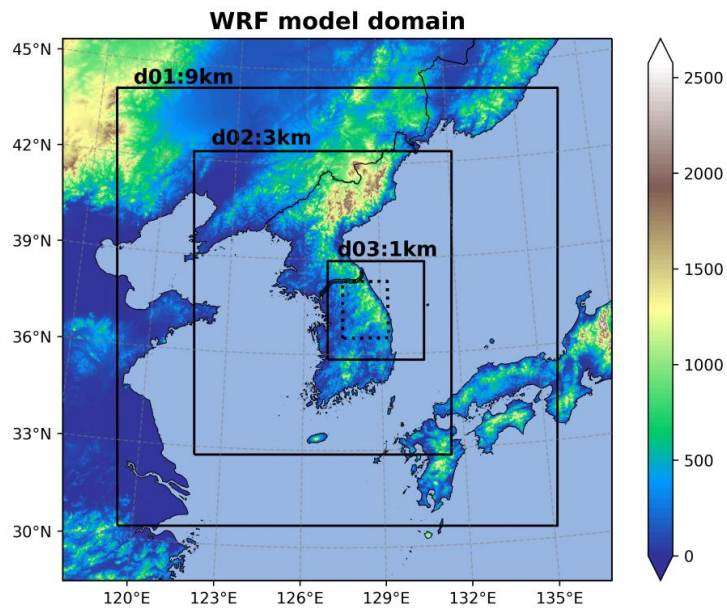
736 **Figure 3.** Area of hydrometeor types in which hourly average fraction of hydrometeors is larger than the
737 threshold indicated. Hydrometeor types are derived from X-band Doppler dual-polarization radar (MXPoL)
738 along the cross-section between MHS and GWU sites at (a) 10 UTC 22 Jan (CASE 3), (b) 23 UTC 07 Mar
739 (CASE 6), and (c) 14 UTC 15 Mar (CASE 7). Eight hydrometeor categories such as crystal (CR), aggregate
740 (AG), rimed particle (RP), ice hail/graupel (IH), melting hail (MH), wet snow (WS), light rain (LR), and rain
741 (RN) are identified. The flows along the cross-section, retrieved from multiple Doppler radars, are also drawn
742 in each figure and the vertical component of the arrows are upward air motion. The flows and classified
743 hydrometeors are the hourly averaged ones .

744
745





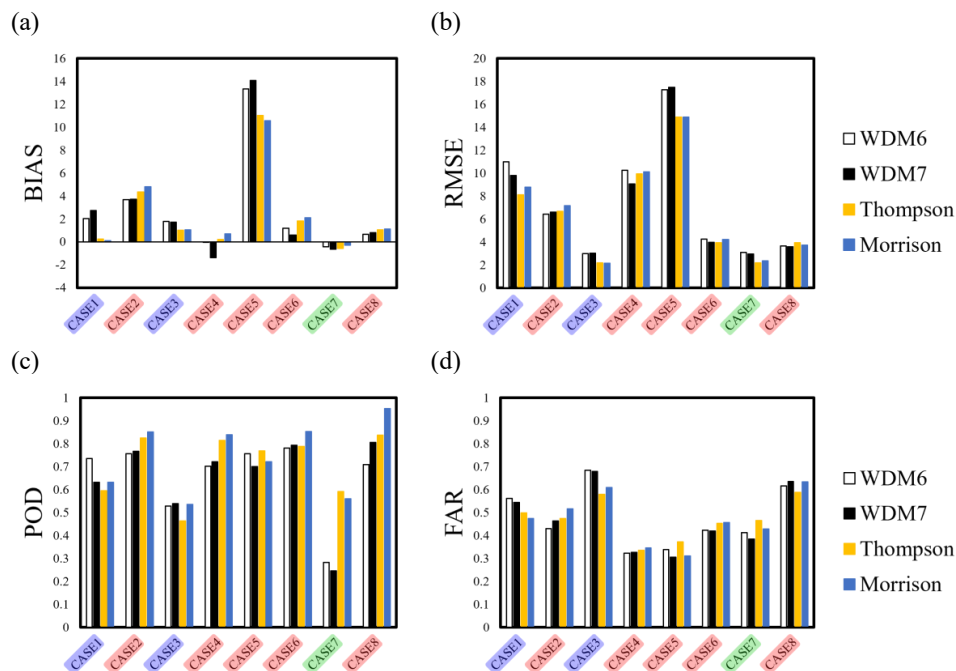
746 **Figure 4.** Model domain consisted of the three nested domains with 9-3-1-km resolutions centered on the
747 Korean peninsula. Shading indicates the terrain height [m] above the sea level and latitudes and longitudes
748 are denoted in the margins. The analysis domain is denoted with a dotted square inside of the innermost
749 domain, d03.



750
751

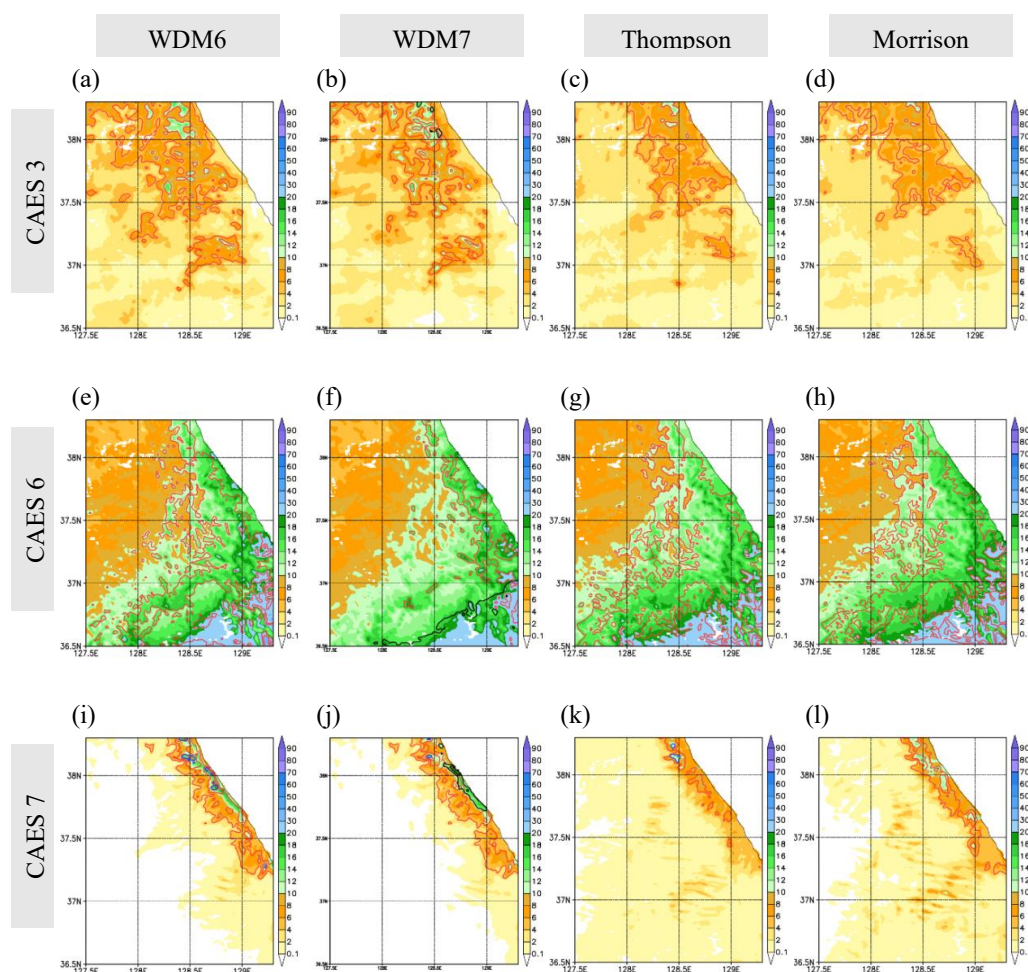


752 **Figure 5.** Statistical skill scores of bias, root mean square error (RMSE), probability of detection (POD), and
 753 false alarm ratio (FAR) for the simulated precipitation, with respect to the AWS observation. The units of bias
 754 and RMSE shown in Figures 5(a) and (b) are [mm]. White, black, yellow, and blue-colored bars represent the
 755 results for the simulations with the WDM6, WDM7, Thompson, and Morrison schemes. The cold-low, warm-low, and
 756 air-sea interaction cases are shaded in blue, red, and green color.
 757
 758



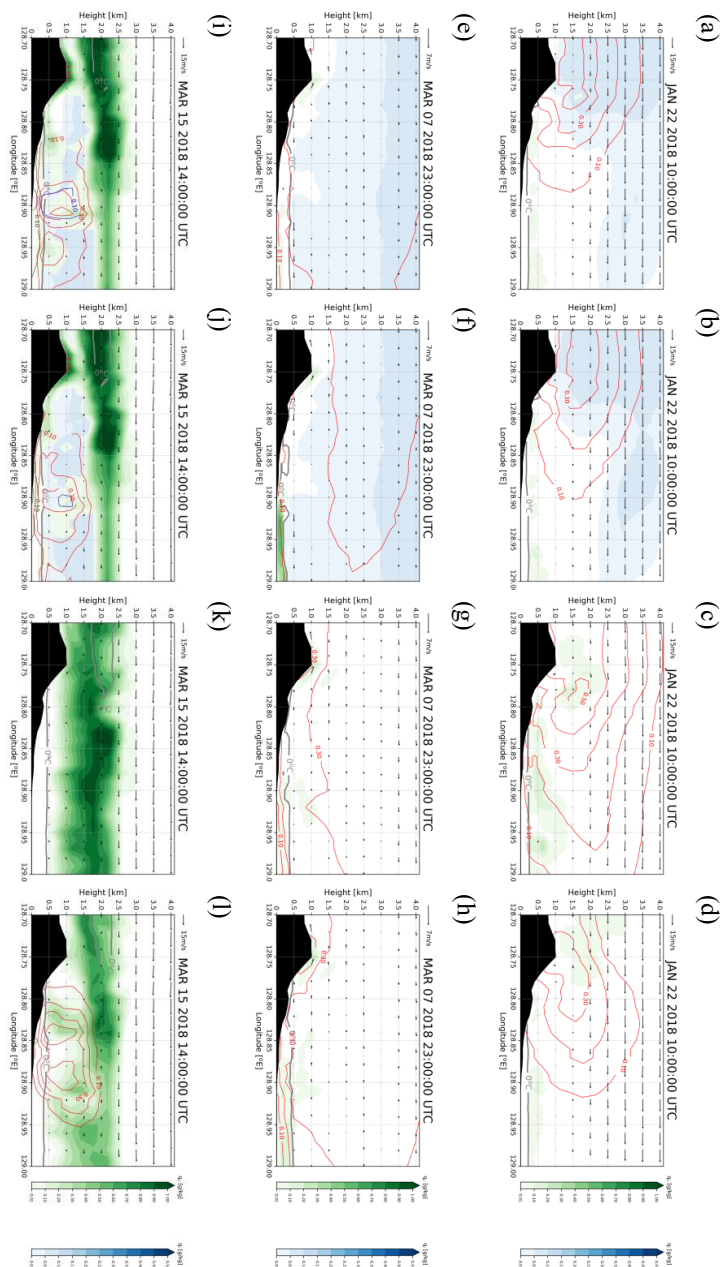


759 **Figure 6.** Accumulated precipitation [mm] of the simulations using different cloud microphysics
760 parameterizations during the analysis period. (a)–(d) are for CASE 3, (b), (e) for CASE 6, and (f) for
761 CASE 7 during the analysis period. (a)–(d) are for CASE 3, (e)–(h) for CASE 6, and (j)–(l) for CASE7. The
762 simulations in the first and second columns are conducted with the WDM6 and WDM7 schemes. The ones in
763 the third and fourth columns are conducted with the Thompson and Morrison schemes. Red, blue, and black
764 contours represent the snow, graupel, and hail-type precipitation at the surface. The contour intervals for snow,
765 graupel, and hail are 5, 10, and 3 mm.
766
767



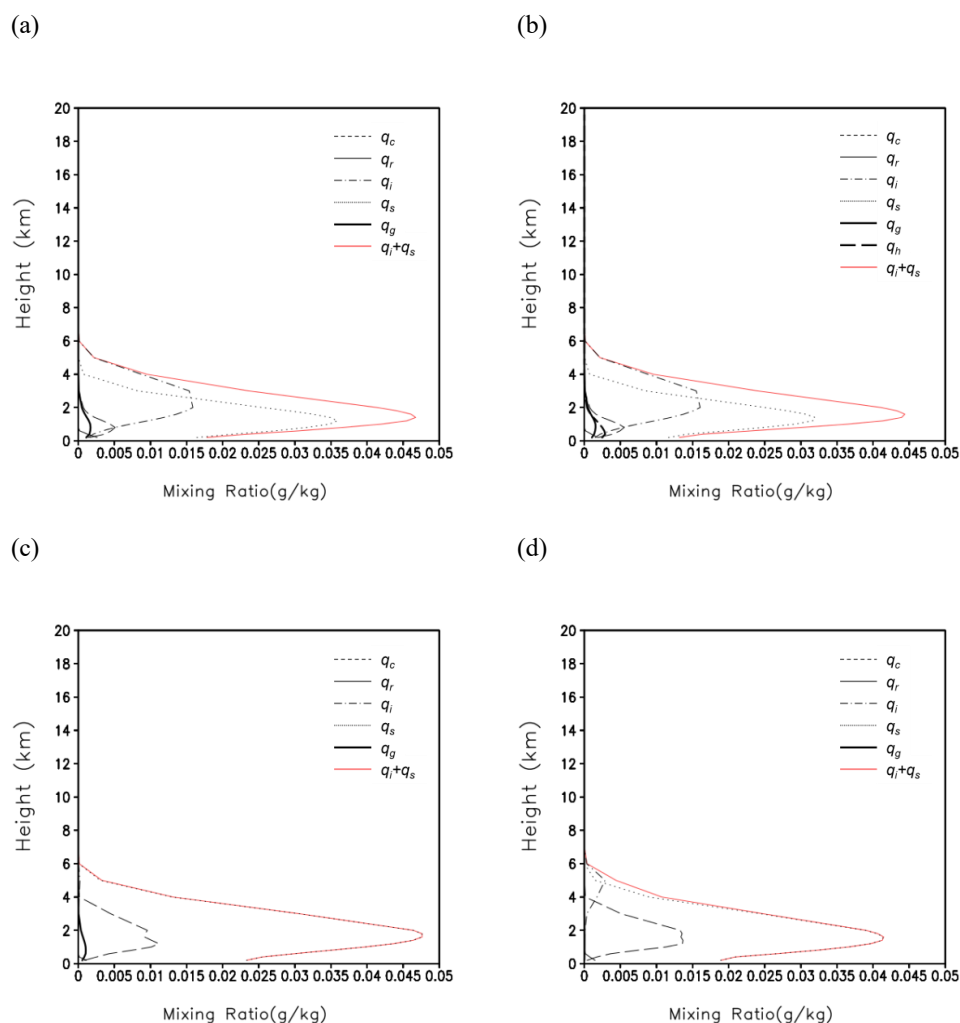


768 **Figure 7.** Terrain and the simulated hydrometeor mixing ratio along the cross-section between GWU and
 769 MHS sites for (a)–(e) CASE 3, (f)–(j) CASE 6, and (k)–(o) CASE 7. From the left column, figures indicate
 770 the simulation results with the WDM6, WDM7, Thompson, and Morrison schemes. Shaded green and blue
 771 indicate the cloud water and ice mixing ratios, respectively. Red, blue, and black-solid contours are for the
 772 snow, graupel, and hail mixing ratios. The contour levels are in 0.1 g kg^{-1} increments and the contour labels
 773 are in $0.1\text{--}0.2 \text{ g kg}^{-1}$ increments. The gray solid line represents the 0°C line. The wind fields are overlaid at
 774 the same time.
 775
 776





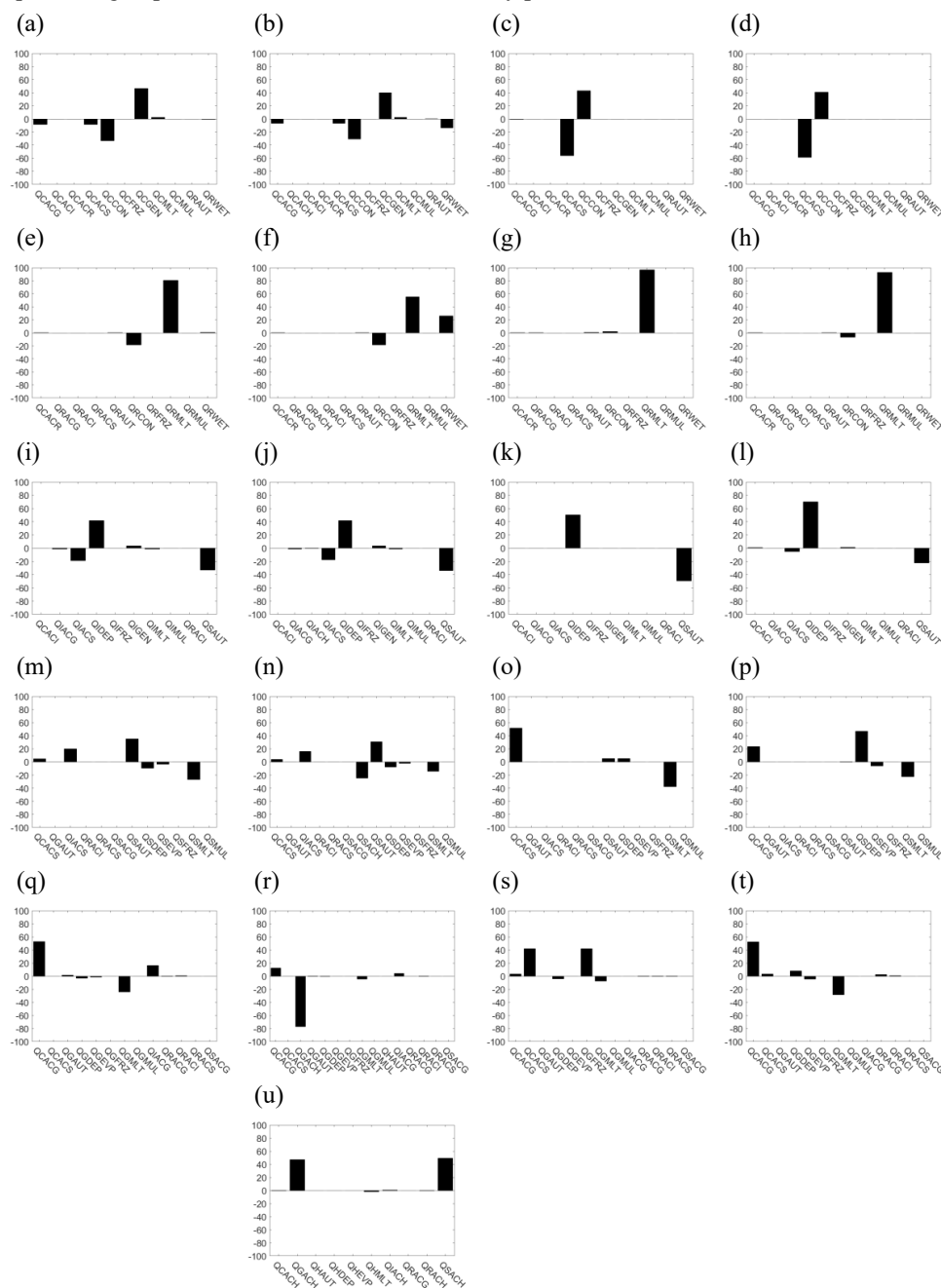
777 **Figure 8.** Time-domain averaged vertical hydrometeor mixing ratio profiles from the simulations using (a)
778 WDM6, (b) WDM7, (c) Thompson, and (d) Morrison schemes for CASE 3. The averaged time and domain
779 are the same as Figure 6. The sum of snow and cloud ice mixing ratios is drawn with a red line in all
780 simulations.
781
782





783 **Figure 9.** Relative contribution of time-domain averaged production term during the analysis period. From
 784 the left column, figures indicate the simulation results with the WDM6, WDM7, Thompson, and Morrison
 785 schemes. (a)–(d) are the terms for cloud water, (e)–(h) for rain, (i)–(l) for cloud ice, (m)–(p) for snow, and
 786 (q)–(t) for graupel, and (u) for hail. The hail is only predicted in WDM7.

787
 788

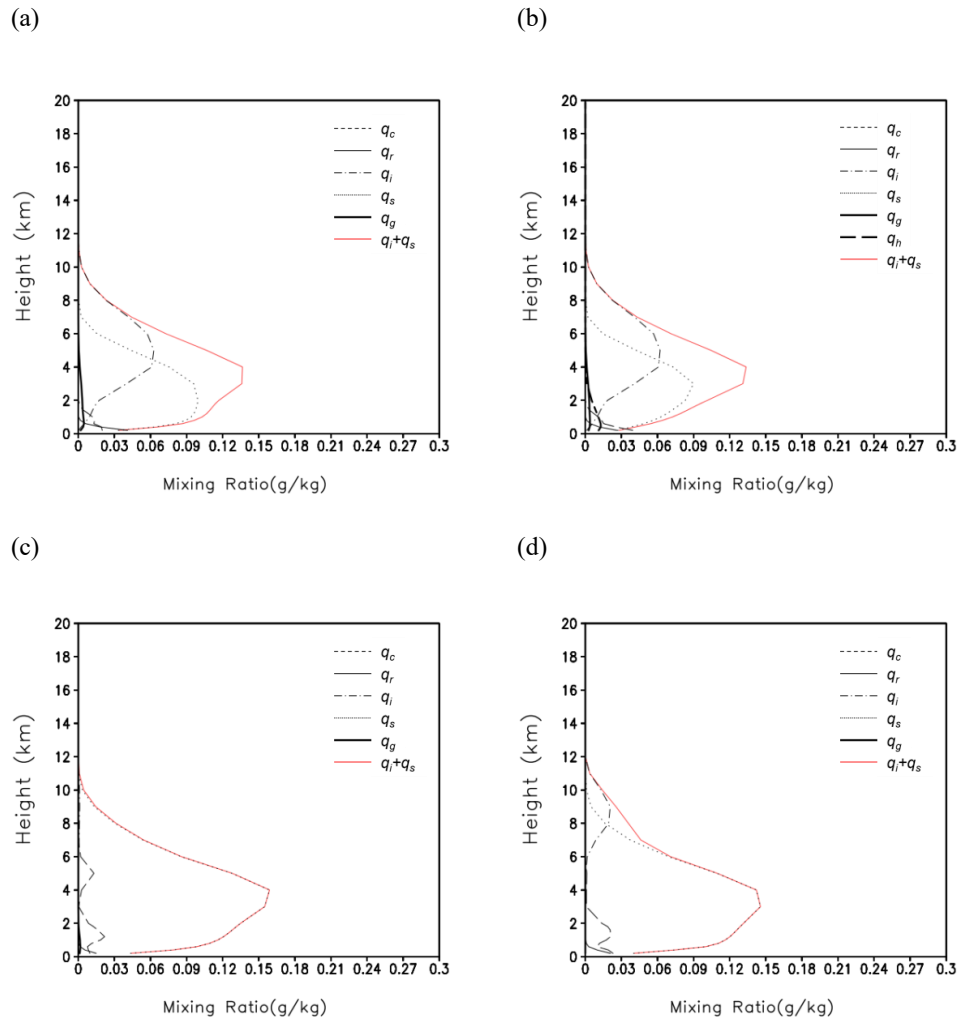




789 **Figure 10.** Same as Figure 8 but representing the results for CASE 6.

790

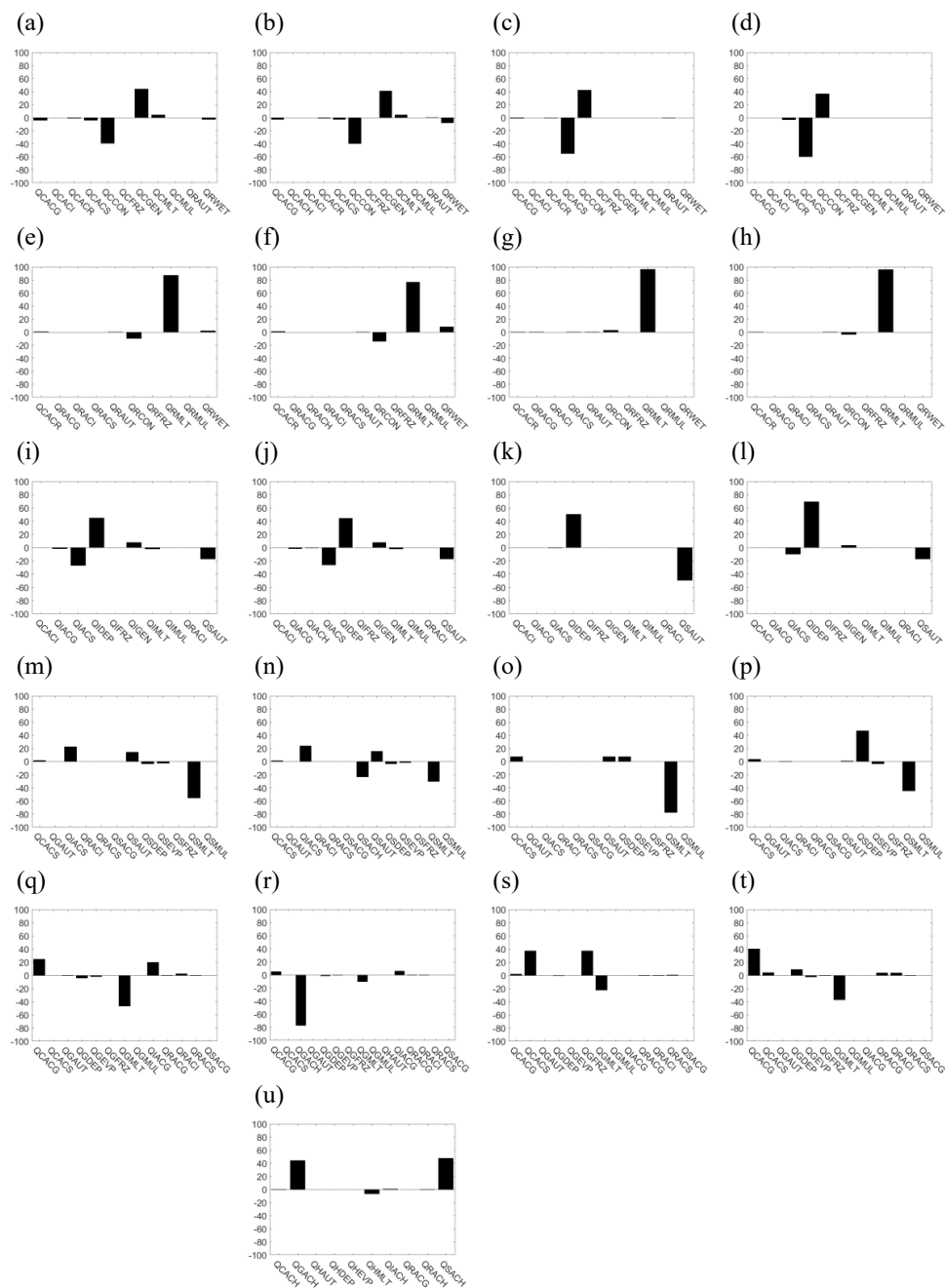
791





792 **Figure 11.** Same as Figure 9 but representing the results for CASE 6.

793
 794

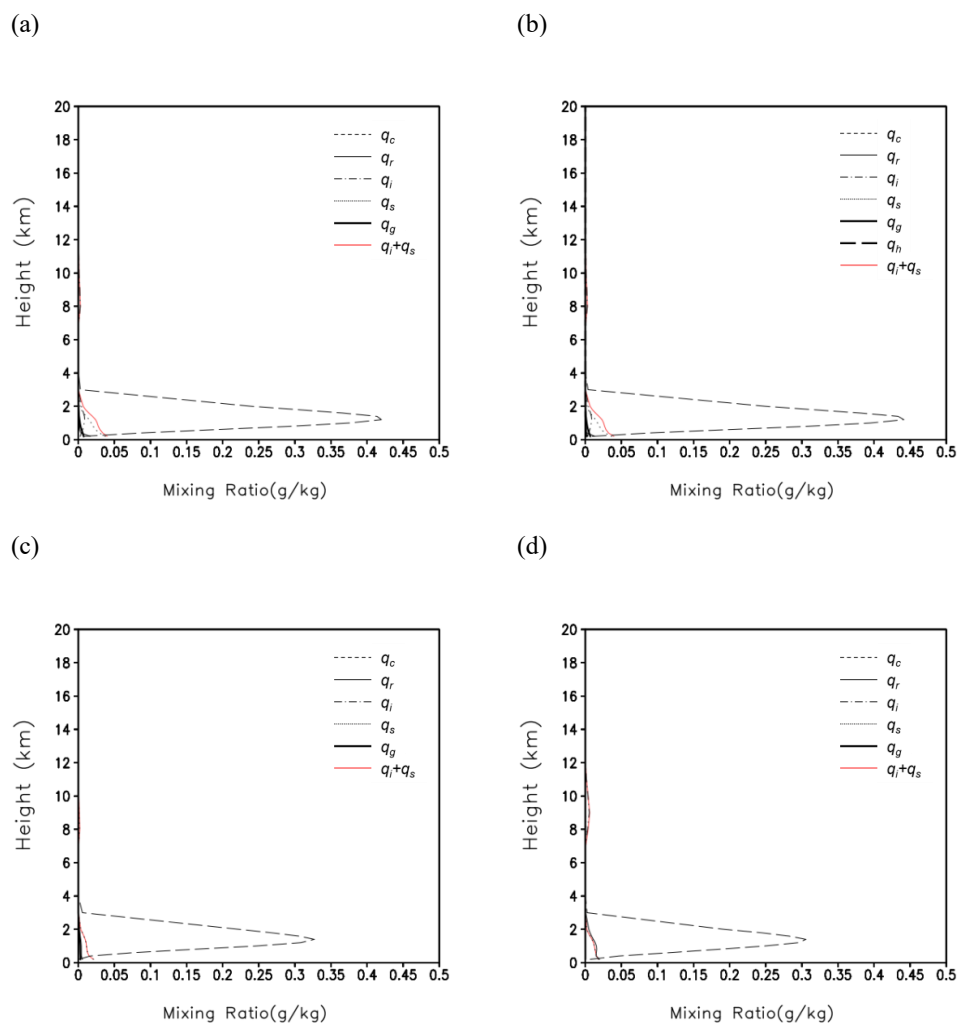




795 **Figure 12.** Same as Figure 8 but representing the results for CASE 7.

796

797





798 **Figure 13.** Same as Figure 9 but representing the results for CASE 7.

799
 800

